RESEARCH ARTICLE SUMMARY

DEVELOPMENT

Temporal variability and cell mechanics control robustness in mammalian embryogenesis

Dimitri Fabrèges*, Bernat Corominas-Murtra*, Prachiti Moghe, Alison Kickuth†‡, Takafumi Ichikawa, Chizuru Iwatani, Tomoyuki Tsukiyama, Nathalie Daniel, Julie Gering, Anniek Stokkermans, Adrian Wolny, Anna Kreshuk, Véronique Duranthon, Virginie Uhlmann§, Edouard Hannezo*, Takashi Hiiragi*

INTRODUCTION: Living organisms, despite their intrinsic variabilities and dynamics, establish robust forms and functions through complex interactions between molecules, cells, and tissues. Molecular and cellular variability has been considered detrimental and is actively minimized by regulatory mechanisms. However, recent studies suggest that variability plays a crucial role in cellular decision making and robustness, including in bacteria, cancer adaptation, tissue differentiation, and embryogenesis. Because early mammalian embryos exhibit variability in gene expression, cleavage timing, and various mechanical parameters, they offer an excellent model to study how variability affects developmental processes.

RATIONALE: Understanding the role of variability in development requires quantification in both space and time [three-dimensional (3D) plus time imaging], and experimental perturbation of variability. This study develops experimental and theoretical methods to quantify morphogenetic reproducibility in early mammalian embryogenesis. We characterized cleavage timing variability in mouse preimplantation embryos and compared it across different mammalian species. We also established a pipeline to segment cell membranes. Using exponential splines, we aimed to provide a rigorous and unbiased method for extracting geometrical information as well as the underlying topological structure of the embryos. This offers an exhaustive yet simple method to quantify and classify the complex dynamics of embryogenesis. Further, we developed an experimental system to examine how temporal variability influences the geometry and topology of embryos during early development. By examining the 3D geometrical and topological structures of cell packings, we sought to identify mechanisms driving the reduction of spatial variability.

RESULTS: The study found that variability in cleavage timing increases at a constant, species-specific rate during the first cleavages in mouse, rabbit, and monkey embryos. This temporal variability was not regulated and possibly contributes to the large morphological variability observed at the beginning of the 8-cell stage. Despite this, the embryos exhibited a notable spatial convergence at the end of that stage. We developed a computational pipeline based on dimensionality reduction and morphomaps to quantify in an unbiased manner the spatial dynamics of embryos, showing that their shape increases in similarity as development progresses. We show that these complex datasets can be interpreted intuitively by considering the topology of the cell packings, showing a convergence in shape mirroring a convergence toward a few rigid topologies. Our physical model indicated that surface energy minimization during compaction was sufficient to drive this convergence, promoting specific topological structures of lower energy and leading to reduced spatial variability. Additionally, we showed that although the zona pellucida encapsulating the embryo is not required for convergence, it reduces the initial set of possible topologies, thus allowing for faster convergence toward the most optimal configuration. Although the packing was maintained from one stage to the next with the natural desynchronization of cleavage timings, experimental synchronization at the 8- to 16-cell stage led to patterning defects in the blastocyst, highlighting the importance of temporal variability for proper development.

CONCLUSION: The findings reveal distinct mechanisms that lead to low spatial variability between different embryos. First, stochastic variability in cleavage timing plays a key role in achieving consistent developmental outcomes across species. Second, surface energy minimization and compaction select a few configurations with minimal energy and drive topological transitions toward these packings, leading to geometrical convergence and a reduction of spatial variability. A third mechanism may involve the zona pellucida constraining the range of potential structures of the early embryo packing. Altogether, these mechanisms ensure robustness in mammalian embryogenesis and present the potential adaptive benefits of stochastic processes in biological systems. ■

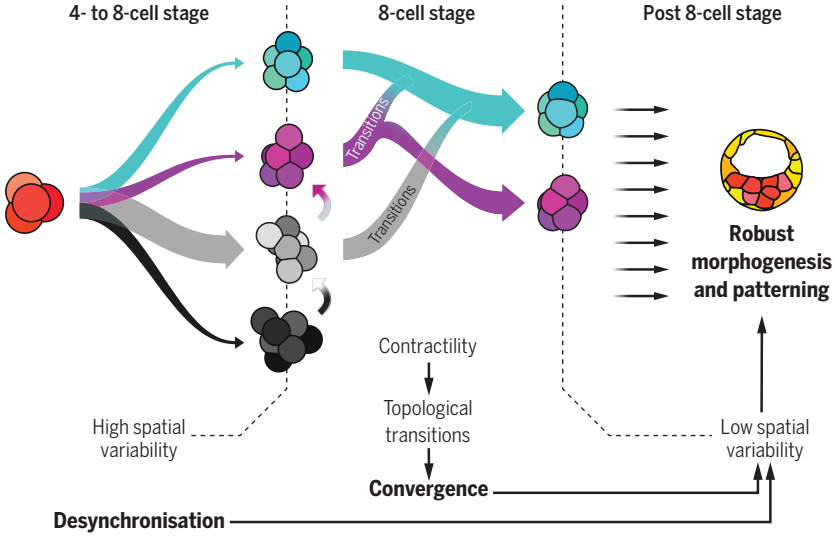

Model of robustness in embryogenesis from cell mechanics and desynchronization. 4-cell stage embryos give rise to many shapes at the beginning of the 8-cell stage, during which cell contractility triggers topological transitions. Ultimately, embryos are driven toward the most optimal packing (cyan). In parallel, the cell-autonomous desynchronization progressively increases temporal variability and helps to maintain topological optimality through generations, lowering spatial variability and promoting robustness.

The list of author affiliations is available in the full article online.
***Corresponding author. Email: d.fabreges@hubrecht.eu (D.F.); bernat.corominas-murtra@uni-graz.at (B.C.M.); edouard.hannezo@ist.ac.at (E.H.); t.hiiragi@hubrecht.eu (T.H.)**
†Present address: Cluster of Excellence Physics of Life, TU Dresden, Dresden, Germany.
‡Present address: Max Planck Institute of Molecular Cell Biology and Genetics, Dresden, Germany.
§Present address: BioVisionCenter Universität Zürich, Zürich, Switzerland.
Cite this article as D. Fabrèges *et al.*, *Science* 386, eadh1145 (2024). DOI: 10.1126/science.adh1145

READ THE FULL ARTICLE AT
https://doi.org/10.1126/science.adh1145

RESEARCH ARTICLE

DEVELOPMENT

Temporal variability and cell mechanics control robustness in mammalian embryogenesis

Dimitri Fabrèges[1,2]*, Bernat Corominas-Murtra[3]*, Prachiti Moghe[1,2], Alison Kickuth[2]†‡, Takafumi Ichikawa[4,5], Chizuru Iwatani[6], Tomoyuki Tsukiyama[4,6], Nathalie Daniel[7], Julie Gering[1], Anniek Stokkermans[1], Adrian Wolny[8], Anna Kreshuk[8], Véronique Duranthon[7,9], Virginie Uhlmann[10]§, Edouard Hannezo[11]*, Takashi Hiiragi[1,2,4,5]*

How living systems achieve precision in form and function despite their intrinsic stochasticity is a fundamental yet ongoing question in biology. We generated morphomaps of preimplantation embryogenesis in mouse, rabbit, and monkey embryos, and these morphomaps revealed that although blastomere divisions desynchronized passively, 8-cell embryos converged toward robust three-dimensional shapes. Using topological analysis and genetic perturbations, we found that embryos progressively changed their cellular connectivity to a preferred topology, which could be predicted by a physical model in which actomyosin contractility and noise facilitate topological transitions, lowering surface energy. This mechanism favored regular embryo packing and promoted a higher number of inner cells in the 16-cell embryo. Synchronized division reduced embryo packing and generated substantially more misallocated cells and fewer inner-cell–mass cells. These findings suggest that stochasticity in division timing contributes to robust patterning.

Living systems rely on molecular and cellular mechanisms with intrinsically stochastic dynamics. Nonetheless, they establish robust forms and functions on multiple scales with complex interplay between molecules, cells, tissues, and species across evolutionary time. Cell organization and decision making have been largely considered instructive, i.e., a signal instructs the recipient cell to differentiate or trigger some signaling pathway (*1*), which may lead to the conclusion that variability is destructive and must be reduced or filtered out. However, it remains unknown whether robust mechanisms and decision making have been evolutionarily selected to accommodate stochasticity or if the processes at the source of variability have been selected to grant robustness. The past decades have shown a growing interest in decision-making paradigms based on stochastic dynamics (*2*–*5*), particularly in bacteria in which gene expression variability was successfully manipulated to demonstrate its role in cell differentiation (*6*, *7*). Stochastic processes have since been shown to be involved in a wide variety of context and species, including cell fate specification (*6*–*12*), cancer adaptation (*13*–*17*), embryo morphogenesis (*18*, *19*), leaf formation (*20*, *21*), tissue folding (*22*), cell sorting (*23*), and evolvability (*24*–*27*).

Early mammalian embryos have been shown to exhibit intra- and inter-embryo variability in gene expression (*10*, *28*–*30*), making them an excellent model to study the role of variability in a minimal and robust system. Gene expression, as well as other mechanical and temporal parameters, exhibit measurable variability within and between embryos that may affect patterning and morphogenesis. For instance, the second cleavage orientation has been shown to be random (*31*); the variability in cleavage timing has been suggested to affect cell fate segregation (*32*, *33*); the nuclear-cytoplasmic ratio has been linked to cell differentiation (*34*); and heterogeneity in cell contractility has been shown to drive cell sorting in the 16-cell stage mouse embryo (*35*, *36*), whereas cell-to-cell variability in cellular fluidity may contribute to the segregation of primitive endoderm and epiblast in blastocysts (*23*). Although recent studies in mice have shown that at least some of these variabilities are regulated by the feedbacks between cell polarity, tissue mechanics, and gene expression (*35*, *37*), the role that intercellular variabilities may play in development and its robustness remains unclear.

To formally address the role of variability, it needs to be quantified with an adequate number of samples suitable for statistical analyses and tested with its manipulation in space and/or time. We thus developed such an experimental system using mouse preimplantation embryos. While spatial organization of development is relatively well-studied in the context of morphogenesis and patterning, less is known about the temporal regulation of developmental progression. We thus started characterizing and measuring the variability among cells in developmental timing.

Embryo variability in cleavage timing increases at a constant and species-specific rate

To characterize the variability of the developmental timing of preimplantation mouse embryos, we first measured the natural variability in cleavage timing between cells within an embryo (Fig. 1A and movie S1). The cell cycles and cleavages of mammalian embryos run asynchronously among blastomeres (*38*) but their variability and potential correlation have not been characterized quantitatively. The duration of the third cleavage (4- to 8-cell stage), for example, ranged from 30 min to 3 hours depending on the embryo, accompanied by variable duration of the inter-mitotic period [Pearson correlation $R = -0.401$ ($P < 0.05$)] (fig. S1A). To assess whether the timing of divisions is actively regulated or coordinated among cells, we built a semiautomatic cell tracking pipeline and quantified cleavage timing in 28 embryos, from the 4- to the 32- or 64-cell stage (Fig. 1, B and C). For this, we challenged the null hypothesis that cells do not show any coordination: Assuming the cell cycle length follows a normally distributed random variable of variance σ_0^2, the successive accumulation of mitosis timing differences should be normally distributed as well, with variance linearly increasing with the cleavage number (Fig. 1D). Deviation from a normal distribution or deviation from the linear relationship between variance and cleavage number would be indicative of an active synchronization or desynchronization influenced by the cell's nearby environment (fig. S1B). In line with the null hypothesis, the distribution of the division timing measured for the third, fourth, fifth, and sixth cleavage followed a normal distribution (Fig. 1E and fig. S1, C and D) and linearly correlated with the cleavage number [Pearson correlation $R = 0.987$ ($P < 0.05$)] (Fig. 1F). Although the average cell cycle length increased after the fifth cleavage (+1 hour, fig. S1E), owing to a longer cell cycle for the cells of the prospective inner cell mass (ICM) compared to the cells of the prospective trophectoderm (TE) (1.5 hours of difference, fig. S1F), as well as a change in the desynchronization dynamics in ICM-fated

[1]Hubrecht Institute, Utrecht, Netherlands. [2]Developmental Biology Unit, European Molecular Biology Laboratory, Heidelberg, Germany. [3]Institute of Biology, University of Graz, Graz, Austria. [4]Institute for the Advanced Study of Human Biology (WPI-ASHBi), Kyoto University, Kyoto, Japan. [5]Department of Developmental Biology, Graduate School of Medicine, Kyoto University, Kyoto, Japan. [6]Research Center for Animal Life Science, Shiga University of Medical Science, Shiga, Japan. [7]UVSQ, INRAE, BREED, Paris-Saclay University, Jouy-en-Josas, France. [8]Cell Biology and Biophysics Unit, European Molecular Biology Laboratory, Heidelberg, Germany. [9]École Nationale Vétérinaire d'Alfort, BREED, Maisons-Alfort, France. [10]EMBL-EBI, Wellcome Genome Campus, Hinxton, UK. [11]Institute of Science and Technology Austria, Klosterneuburg, Austria.
***Corresponding author. Email: d.fabreges@hubrecht.eu (D.F.); bernat.corominas-murtra@uni-graz.at (B.C.M.); edouard.hannezo@ist.ac.at (E.H.); t.hiiragi@hubrecht.eu (T.H.)**
†Present address: Cluster of Excellence Physics of Life, TU Dresden, Dresden, Germany.
‡Present address: Max Planck Institute of Molecular Cell Biology and Genetics, Dresden, Germany.
§Present address: BioVisionCenter Universität Zürich, Zürich, Switzerland.

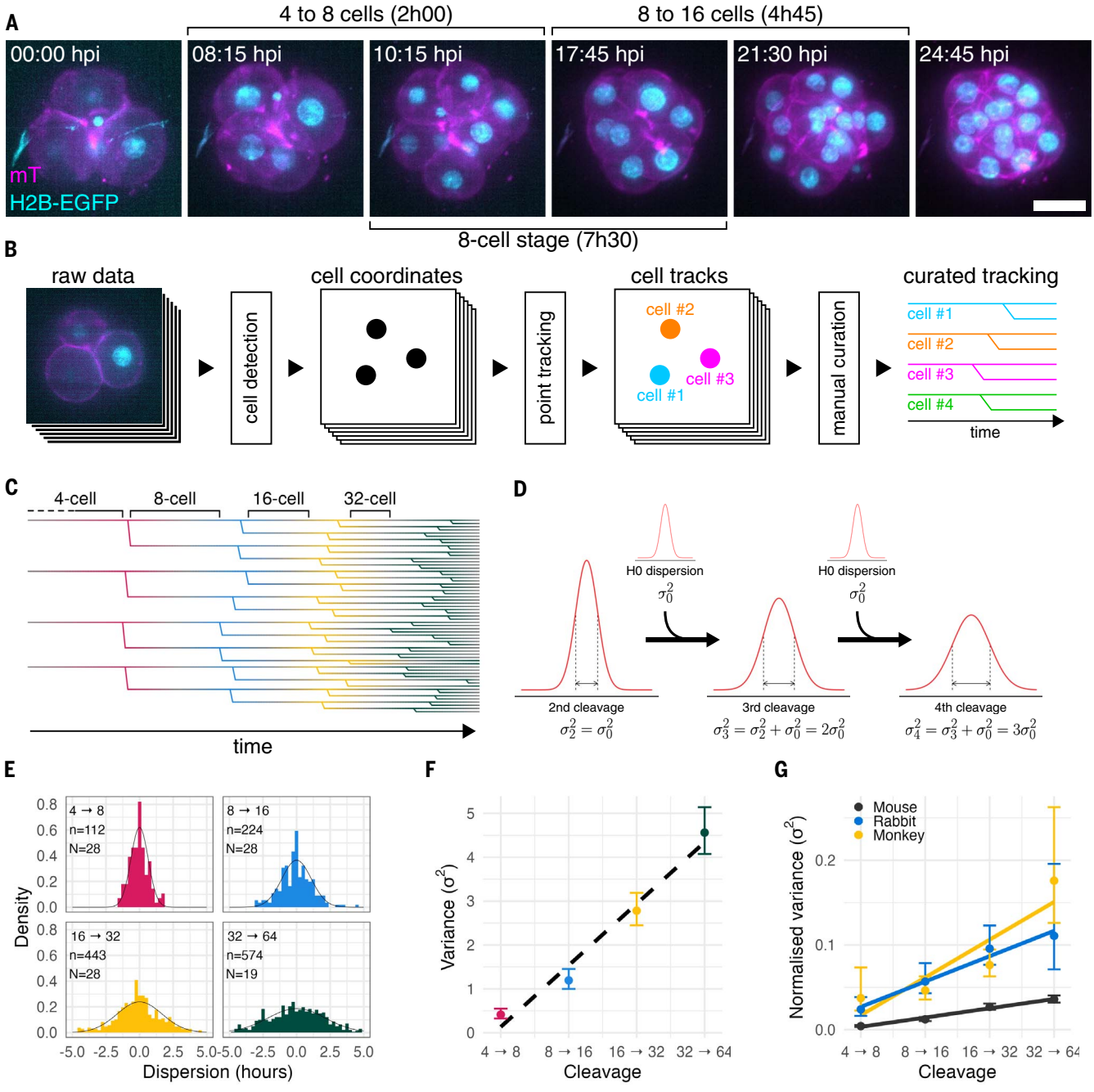

Fig. 1. Embryo variability in cleavage timing increases at a constant and species-specific rate. (**A**) Maximum intensity projection of a representative live imaging dataset (out of 28 embryos and eight independent experiments), of a mouse embryo expressing mT (magenta); H2B-EGFP (cyan). Time after imaging (hh:mm); scale bar, 25 μm; see also movie S1. (**B**) Schematic representation of the processing pipeline. 3D+time microscopy data were analyzed to automatically detect nuclei coordinates, then tracked and manually curated; see also Materials and Methods. (**C**) Representative tracking displaying the third (pink), fourth (blue), fifth (yellow), and sixth (green) cleavages over a period of 43 hours, from left to right. Each branch is a cell and each branching is a mitosis. (**D**) Schematic representation of the null hypothesis (H0) under which the distribution of the timing of mitosis at the n^{th} cleavage is normally distributed with a variance of σ_n^2 and equals the cumulative sum of independent normally distributed random variables with a variance of σ_0^2 such that $\sigma_n^2 = (n-1)\sigma_0^2$. See also fig. S1B. (**E**) Density distribution of the timing of mitosis around the mean for the third, fourth, fifth, and sixth cleavages. Black line, Gaussian fit. n, number of mitoses; N, number of embryos. Color code same as in (C). (**F**) Variance in mitosis timing as a function of cleavage number. Dashed line indicates linear regression. Pearson correlation R = 0.987, P = 0.013, $CI_{95\%}$ = [0.493; 1.000]. Color code same as in (C). (**G**) Comparison of the variance of mitosis timing normalized by the cell cycle length, as a function of the cleavage number in mouse (black, 28 embryos from eight independent experiments), rabbit (blue, 11 embryos from four independent experiments) and monkey (yellow, 12 embryos from four independent experiments). Thick lines indicate linear regression. Pearson correlation R_{mouse} = 0.993, R_{rabbit} = 0.987, R_{monkey} = 0.906. Pairwise F-test: P-value < 10^{-7} for mouse versus rabbit and mouse versus monkey at all cleavages; P-value > 0.05 (nonsignificant) for rabbit versus monkey at all cleavages. Error bars, 95% confidence interval (CI).

cells (fig. S1G), we did not find significant correlation between cell relative position and relative timing of division (fig. S1H). This suggests that the lengthening of the cell cycle and the slower desynchronization pace in ICM-fated cells compared with TE-fated cells was a consequence of cell differentiation and not direct cell-cell spatial interaction. To confirm this, we introduced a substantial asynchrony in the cleavage timing by inserting a time-shifted, one-eighth blastomere under the zona pellucida (ZP) of host embryos at the 8-cell stage, effectively generating a 9-cell heterochronic chimera (fig. S1I). In this experiment, we split the embryos into two groups based on the average mitosis timing of the cells during the third cleavage. The time difference between the two groups was between 2.5 and 7 hours. Under the hypothesis that cells actively communicate to adjust their timing of division, we expected the cell from the donor and/or the cells from the host to adjust their timing of division and control the degree of asynchrony. However, we did not observe a change in the time shift between the donor cell and the cells of the host during the following cleavages (fig. S1J). Instead, the time difference was maintained, indicating that substantial perturbation in cleavage timing is not compensated. These observations indicate a lack of discernible cell-cell coordination in cleavage timing, which results in a cell-autonomous, but cell-fate–dependent, desynchronization at a constant rate.

Because various mammalian embryos undergo asynchronous cleavage cycles, we performed a similar characterization of variability in division timing of embryos expressing fluorescent tags. We injected rabbit embryos with mRNA encoding for a cell membrane–localized coral-derived fluorescent protein TagRFP-T (myrTagRFP-T) and mRNA encoding for the chromatin-localized Histone H2B protein fused with the enhanced green fluorescent protein (H2B-EGFP) (fig. S1K and movie S2). We injected monkey embryos with an mRNA encoding for a cell membrane-localized tdTomato (mT) fused with H2B-EGFP by the self-cleaving peptide T2A (fig. S1L and movie S3). Live-imaging microscopy and its analysis showed that rabbit and monkey embryos shared a similar desynchronization pattern, with their desynchronization rate higher than that of mouse embryos (Fig. 1J, normalized by cell cycle length, see Materials and Methods and fig. S1M without normalization). Notably, the desynchronization rate was species-specific, which suggests that variability in cleavage timing may be an evolutionary trait that plays a role in the following developmental processes.

Embryo spatial variability decreases during the 8-cell stage

To investigate the impact of the variability in cleavage timing on the robustness of development, we developed a pipeline to parameterize cell shape and build a statistical vector map of morphogenesis, or morphomap (Fig. 2A). First, cells were automatically labeled, followed by manual curation, from three-dimensional (3D) images of transgenic embryos expressing a cell membrane–localized tdTomato (mT). Then, the surface of the labeled objects was fitted with exponential splines (*39*) (see fig. S2, A and B, and Materials and Methods for details), generating a set of 63 parameters describing both the shape of each cell and its relative position in the embryo. Each embryo was thus geometrically described by a set of 63 parameters × 8 blastomeres: 504 parameters, projected in 2D (for visualization only) using a standard t-distributed stochastic neighbor embedding dimensional reduction (t-SNE). The t-SNE 2D-projection of the 504D-morphomap of 29 embryos (Fig. 2B) and the measurement of the corresponding high-dimensional Euclidean distances considering the 446,985 potential pairs between 946 3D-images of embryos during the 8-cell stage revealed that embryos seem to become more and more geometrically similar and converge toward a specific area of the morphomap [Pearson correlation $R = -0.965$ ($P < 10^{-4}$), Fig. 2C and fig. S2C; see also isolines for illustration in Fig. 2B].

Likewise, we built the morphomap for rabbit ($n = 10$, Fig. 2D and fig. S2D) and monkey ($n = 12$, Fig. 2E and fig. S2E) embryos to examine whether their embryos show similar geometrical convergence. Rabbit and monkey embryos were larger in volume than mouse embryos (fig. S2F), hence their total volume was normalized to allow for direct comparison. Notably, the three species exhibited similar geometrical structures and shared the same region of the morphomap as demonstrated by the overlapping clusters in high dimension (silhouette index = 0.029, Fig. 2F). This suggests that similar design principles could govern embryo shape changes during the 8-cell stage in the three species.

In search of such a principle driving geometrical convergence, we looked into compaction. In mouse embryos, compaction starts at the 8-cell stage, which results in significant cell shape changes and an overall smoothing of embryo surface. Using the compaction parameter α [which can be measured directly from the cell-cell contact angles at the fluid interface, fig. S2, G and H, and equal to the ratio between cell-cell and cell-bulk surface tensions (*40*)], we quantified the compaction over time and observed a significant decrease of the α-parameter, indicative of an increase of the degree of compaction and cell shape change (Fig. 2, G and H, and fig. S2G). However, we did not find a correlation between the geometrical distance and the α-parameter [Pearson correlation $R = 0.781$) ($P = 0.1185$, non-significant), Fig. 2I], with an exception for α below 0.4, where the geometrical distance between embryos is significantly smaller, although many embryos did not reach α below 0.4 (Fig. 2H). This suggests that cell shape changes due to compaction are not sufficient to explain the observed convergence.

Embryo topological variability decreases during the 8-cell stage

We reasoned that the morphomap encompasses both shape and arrangement of the cells. While the former is linked to the geometrical changes induced by compaction, the latter depends on the raw cell-cell contact structure, i.e., the topological properties of the embryo packing (*41*–*45*). Thus, to identify the mechanism driving morphological convergence, we examined cellular topology in the 4- and 8-cell-stage embryo. It has been shown that although there is an infinitely large number of 3D geometrical arrangements, four adhesive spheres have only one possible rigid packing and 8 adhesives spheres have only 13 possible rigid packings. A packing is called rigid when no independent movements of cells are possible or, more technically, when any relative cell-cell displacement costs finite energy (*46*–*48*) (Fig. 3A and fig. S3A). We thus used these packings as landmarks to interpret our morphomaps, and classified embryos either as nonrigid (NR) or as belonging to one of the rigid packings, based on the topological proximity of the cell-cell contact structure of the embryo to one of the rigid packings (see Methods for details). Distinct packings were labeled following the Schoenflies notation for 3D crystallographic structures (*49*).

This analysis revealed that although many embryos were NR at the start of the 4- and 8-cell stage, all 4-cell stage embryos quickly converged geometrically and topologically to their specific rigid packing (fig. S3, B and C), whereas nearly all of the 8-cell stage embryos converged toward one of the 13 rigid packings (fig. S3D). Notably, we observed an additional and unexpected topological convergence within rigid packings at the 8-cell stage, as two specific rigid packings, $C_s(2)$ and D_{2d}, became highly overrepresented over time (30.3 and 29.7%, respectively, of 29 embryos, fig. S3D). All the other rigid packings were grouped and referred to as "others" in subsequent analyses. Notably, D_{2d} overlaps with the attractor region detected by our morphospace analysis (Fig. 3B). However, when grouped by embryo packing, the inter-embryo geometric distance was stable over the course of the 8-cell stage (Fig. 3C). This suggests that the geometrical convergence characterized in Fig. 2C may result from successive topological transitions from geometrically diversified packings (NR and "others") to packings exhibiting lower geometrical variability [$C_s(2)$ then D_{2d}]. To test this prediction, we analyzed the evolution

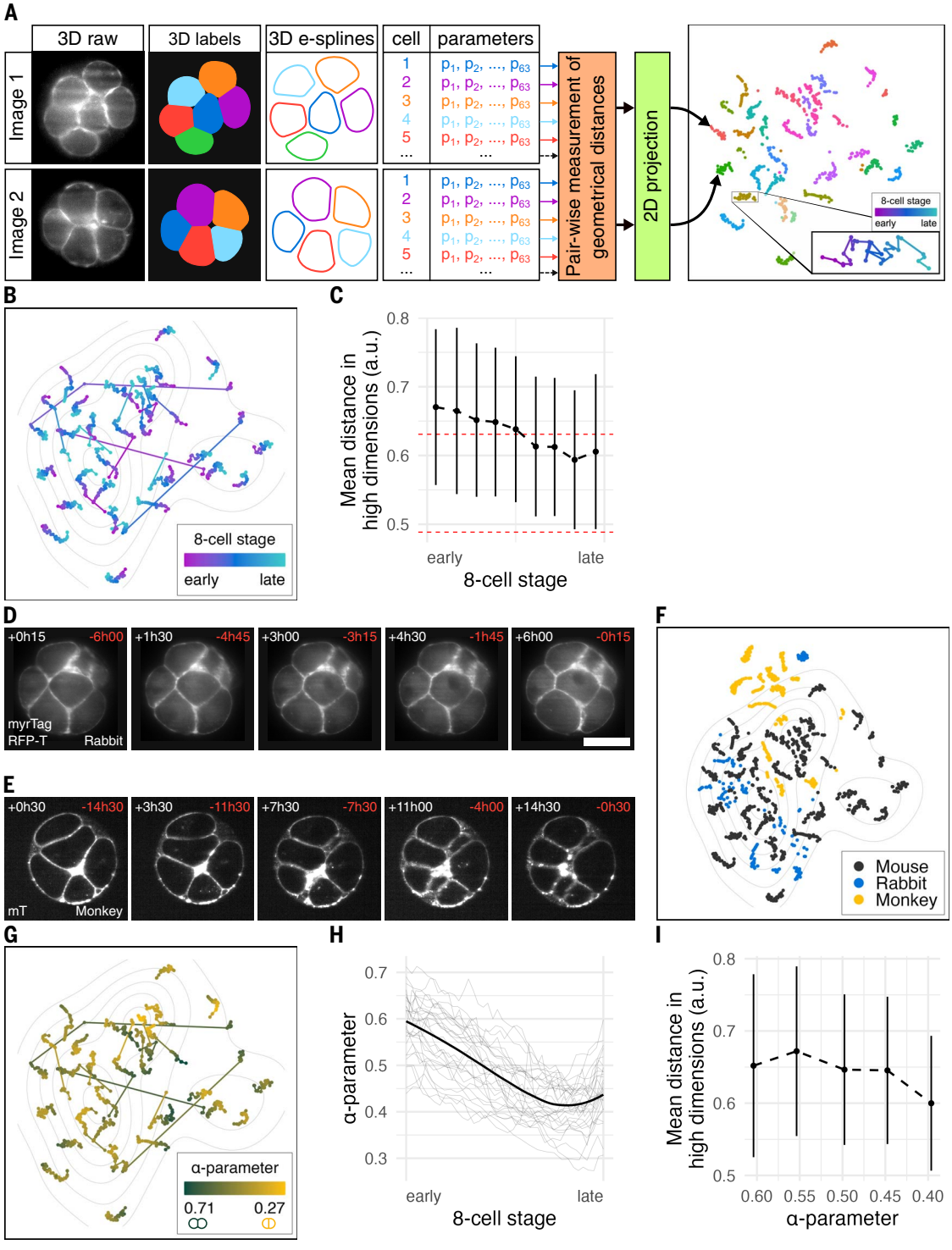

Fig. 2. Embryo spatial variability is reduced during the 8-cell stage. (**A**) Descriptive schematic of the geometrical distance measurement pipeline. (Left to right) 3D images of cell membranes; cell segmentation and curation of labeled volumes; fit with exponential splines; set of 504 parameters for each embryo at each time point. The pairwise distances of all 3D images were computed from the exponential spline parameters and used to project the 504D-morphomap on a 2D plane (see also Materials and Methods, color-coded embryos). (Inset) One embryo trajectory color-coded from the early 8-cell stage (magenta) to late 8-cell stage (cyan). (**B**), (**F**), and (**G**) t-SNE projection. Each embryo is represented with sequence time points and colored as a function of the normalized progression though the 8-cell stage [(B) early in magenta, late in cyan], the species [(F) mouse in black, rabbit in blue, and monkey in yellow], and the compaction parameter [(G) high alpha/low compaction in green, low alpha/high compaction in yellow]. Isolines, density map of the end of the 8-cell stage. Number of embryos: 29 (mouse), 10 (rabbit), and 12 (monkey). (**C**) and (**H**) Normalized time course through the 8-cell stage of the mean ± s.d. of the pairwise geometrical distances (C) and the mean compaction parameter α (H) in 29 embryos. Light gray lines, individual embryo tracks. Red dashed line, reference lines showing a representative high distance (top line, the average geometrical distance between the early shape of an embryo and its final configuration) and a representative low distance (bottom line, the average distance between an embryo and itself 1 hour later). (**D**) and (**E**) Cross section of a representative live imaging dataset of a rabbit embryo [(D) out of 10 embryos from four independent experiments] and a monkey embryo [(E) out of 12 embryos from four independent experiments] expressing myrTagRFP-T (D) and mT (E). Scale bar, 50 μm. Time after the beginning (white, top left corner) and before the end (red, top right corner) of the 8-cell stage. See also fig. S2, D and E. (**I**) Mean ± s.d. of the pairwise geometrical distances as a function of the α-parameter in 29 mouse embryos.

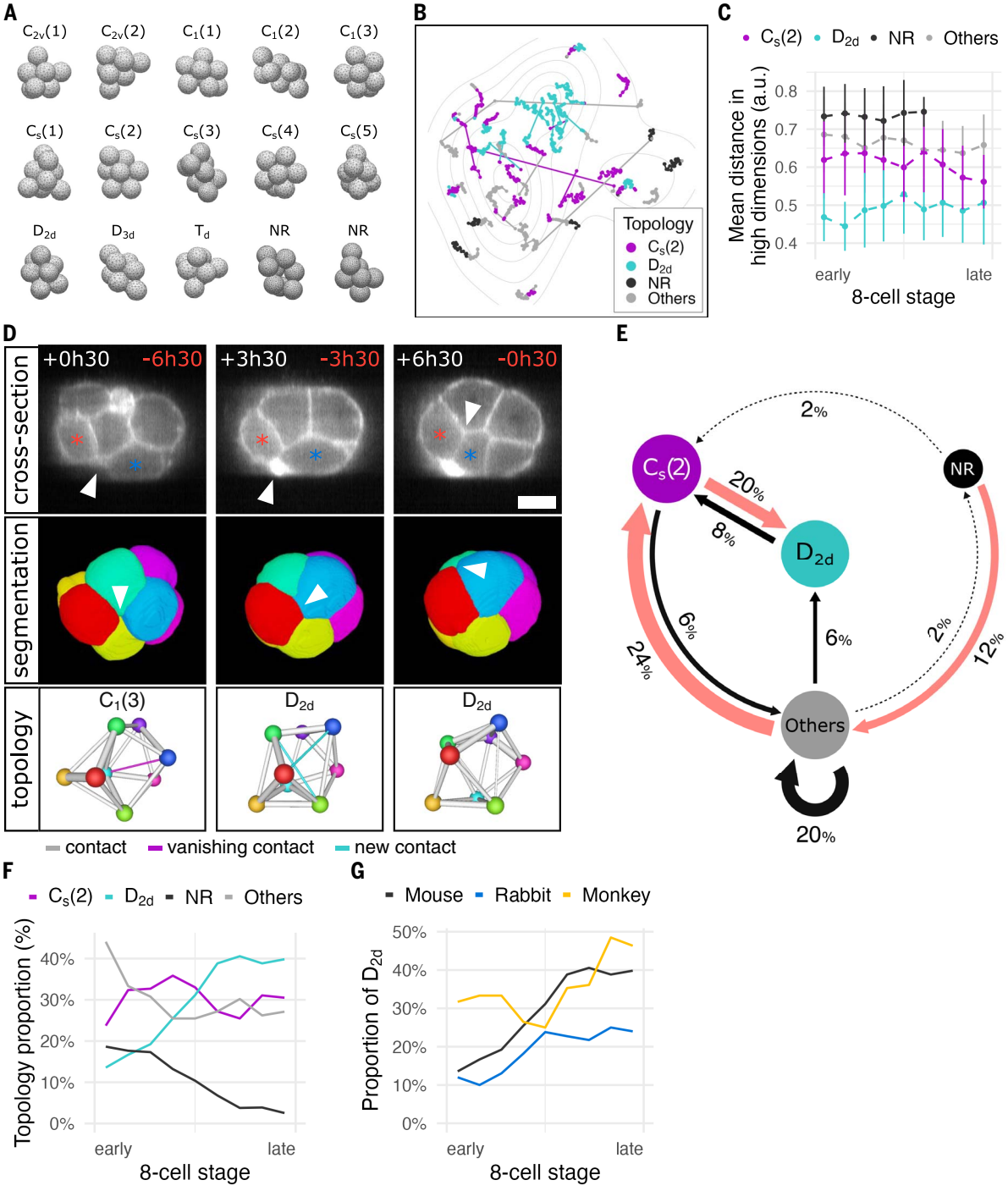

Fig. 3. Embryo topological variability is reduced during the 8-cell stage. (**A**) The 13 rigid packings and two examples of NR packings for clusters of 8 spheres. See also fig. S3A. (**B**) t-SNE projection of the morphomap. Each embryo is represented with a sequence of connected timepoints and colored as a function of the topological proximity to $C_s(2)$ (magenta), D_{2d} (cyan), or any other rigid packing (gray). NR packings are in black. Isolines, density map of the end of the 8-cell stage for visual aid only. n = 29 mouse embryos. (**C**) Normalized time course through the 8-cell stage of the mean ± s.d. of pairwise geometrical distances within embryos grouped and colored as in (B). (**D**) Cross section (top row), cell segmentation (middle row), and topological network (bottom row) of a topological transition from $C_1(3)$ (first column) to D_{2d} (second and third columns). Arrowheads indicate absence (first column), initiation (second column), and expansion (third column) of contact between cells marked by red and blue stars (top row) or in red and blue (middle and bottom rows). Contact loss (magenta) and gain (cyan) are shown on the topology network among lasting contacts (gray). Time in hours after the start (white) and before the end (red) of the 8-cell stage. Scale bar, 25 μm. See also movie S4. (**E**) Topological transition map of 8-cell stage mouse embryos between $C_s(2)$ (magenta), D_{2d} (cyan), NR (black), and other rigid packings (others, gray). Arrows show observed topological transitions (once: dotted; more: solid). Circle area is proportional to topology proportion. Arrows are labeled and sized by transition frequency. Red arrows indicate net transition flux. n = 50 transitions. (**F**) Proportion of $C_s(2)$ (magenta), D_{2d} (cyan), NR (black), and other rigid packings (Others, gray) by the normalized progression through the 8-cell stage. n = 29 mouse embryos. See also fig. S3D. (**G**) Proportion of D_{2d} in mouse (black, n = 29 embryos), rabbit (blue, n = 10 embryos), and monkey (yellow, n = 12 embryos) by the normalized progression through the 8-cell stage. See also fig. S3E.

of the topological transitions over time. Fifty topological transitions were observed from 29 embryos during which cell contacts were created, lost, or strengthened (Fig. 3D and movie S4). Transitions from NR to others, others to others, others to $C_s(2)$ and $C_s(2)$ to D_{2d} were overrepresented (Fig. 3E) resulting in a significant decrease of NR packings described earlier from 18.6 to 2.5% and in an increase of D_{2d} proportion from 13.6 to 39.8% over the course of the 8-cell stage (Fig. 3F). A similar topological transition and distribution was also observed in rabbit and monkey embryos (Fig. 3G and fig. S3E). Collectively, these analyses show that the overall geometrical convergence among mammalian embryos is driven by a chain of topological transitions through $C_s(2)$ toward D_{2d}.

Surface energy minimization with compaction is sufficient to recapitulate geometrical and topological convergence

Although the convergence from NR to rigid packings can be rationalized readily, given that rigid packings correspond to local energy minima of the system, the secondary convergence toward a single packing was less intuitive as all 13 rigid packings have the same energy for attractive hard spheres (*47*). However, this does not necessarily apply to deformable and adhesive cells. Upon compaction, cell-cell adhesion configuration is well-described by a soap bubble model (*35*, *40*, *50*–*53*) in which the relative energy can be determined with the cell-cell contact surface area, the contact-free surface area (not in contact with other cells), and the relative surface tension or α-parameter (Fig. 4A, see also Materials and Methods). To test how cell-cell adhesion and compaction (characterized by the α-parameter) changes the optimal configurations of embryo packings, we used the Surface Evolver software (*54*) to simulate morphogenesis. We tested the theoretical predictions and, in a data-driven manner, checked whether the observed evolution of imaged embryos and their changes in the α-parameter could be captured by the proposed theoretical framework. Using the 13 rigid packings (Fig. 3A) as initial conditions to our model, we simulated the compaction from low to high compaction (α = 0.8 and 0.3 respectively, Fig. 4, B and C and fig. S4, A and B). Crucially, compaction leads to few specific packings having a lower energy than others (with D_{2d} being the lowest, Fig. 4D), and as a consequence, the model predicted a dramatic convergence at high compaction toward D_{2d} for most of the rigid packings (Fig. 4, E and F and fig. S4C). Several of these transitions could occur even with low levels of noise, owing to compaction near-deterministically creating new cell contacts (fig. S4, D and E). Nevertheless, a number of other topological transitions required cell rearrangements (or T1 transitions), which have been shown to be associated to the overcoming of energy barriers across different modeling frameworks (*55*–*58*). In this context, noise acts as a trigger to go from one minimum to another, thereby avoiding the system remaining trapped in suboptimal energy configurations (see Materials and Methods). We also found that $C_s(2)$ was the second most stable packing and functioned as a transition intermediary toward D_{2d} in the simulations. The model thus closely mirrored our experimental datasets for topological transitions toward D_{2d} [largely through $C_s(2)$] observed in 8-cell stage embryo.

To challenge its predictions further and more quantitatively, we compared embryo morphodynamics with their simulated counterparts, by using real embryo geometry and topology at the start of the 8-cell stage as an initial condition to start the simulation (fig. S4F). The model could successfully recapitulate both the transitions from NR to rigid packings as well as the geometrical convergence (Fig. 4G). In particular, we found that the geometrical distance between embryos and their corresponding simulations is significantly smaller than the geometrical distance in random pairs of embryos (Fig. 4H) and corresponds to a typically low distance as shown previously (Fig. 2C, bottom red dashed line). Taken together, our in silico model based on the surface energy minimization was able to recapitulate the 8-cell embryo morphogenesis and predict geometrical and topological convergence to D_{2d}. The attraction to D_{2d} can thus be explained by having the least surface energy for every tested α-parameter (Fig. 4D and fig. S4E), which suggests that with a sufficient amount of time and some level of dynamic changes and fluctuation in cell shape (fig. S4, A and B), all packings would eventually converge to D_{2d} (Fig. 4I).

Compaction and surface contractility drive topological transitions

Our simulations predicted that compaction plays a key role in the convergence toward a well-defined topological structure, by favoring a specific cellular packing as well as lowering barriers for transitions. Consistent with this prediction, we found that the increase in probability toward the D_{2d} topology correlated strongly with the compaction parameter α. (Fig. 5A and fig. S5, A and B), increasing from 0.0% for α = 0.7 to 27.4% for α = 0.6, and from 27.6 to 69.0% for α < 0.45. Although the decrease in α varied considerably from embryo to embryo, the probability of topology correlated much more strongly with α than with time (Fig. 3F), arguing that compaction is a primary driver of the convergence to D_{2d} during the course of the 8-cell stage. To test this functionally, we first generated mT embryos that lack the maternal allele Myh9 (hereafter referred to as mMyh9$^{+/-}$). Because Myh9 is the specific isoform of myosin heavy chain that is required to generate surface tensions, in its absence embryos fail to compact properly and build cortical contractility (*4*) (Fig. 5, B and C, and movie S5). In line with the predictions, mMyh9$^{+/-}$ embryos showed no topological transitions to D_{2d} for compaction parameters even as low as 0.55 (Fig. 5D and fig. S5C), while NR packings were overrepresented throughout the 8-cell stage (mean ± s.d. = 73.9% ± 8.0) and embryos did not converge topologically nor geometrically (Fig. 5E and fig. S5D). Furthermore, using *para*-aminoblebbistatin (PAB, 10 μM), a photostable myosin II inhibitor (*59*), we obtained embryos with a milder effect on compaction and that showed intermediate topological and geometrical outcomes (fig. S5, E to I, and movie S6). Altogether, these findings confirm the predictions of our model and demonstrate that compaction and surface contractility drive topological transitions and spatial convergence in the early mouse embryo.

The ZP restricts the initial morphological space of embryos

We noted, however, that monkey embryos, with apparently smaller perivitelline space in comparison to mice and rabbits (fig. S6A), achieve geometrical and topological convergence despite the negligible compaction at the 8-cell stage (Fig. 6, A and B). This suggests a possible role for the ZP in convergence, and we tested it with two experiments.

First, mechanical removal of the ZP in mouse embryos demonstrated that in the absence of ZP, embryos exhibited a much wider variety of shapes, including topologies [$C_{2v}(1)$ and D_3d] that are otherwise rarely observed, with an overrepresentation of NR structures (Fig. 6C). Importantly, however, we found that as compaction proceeded, ZP-less embryos still displayed morphological convergence, as evidenced by a decrease in high-dimensional Euclidean distances (Fig. 6D) and topological transitions toward rigid packings (Fig. 6C). Our analysis is consistent with the process of convergence toward the same state through intermediaries as embryos with ZP [e.g., $C_s(2)$], but delayed by starting from a broader region of phase space (Fig. 6, E and F). To further evaluate the convergence quantitatively, we introduced a packing parameter that measures the deviation of outer cell surface from a certain distance to the embryo center, inverted such that a high value indicates a more packed embryo (fig. S6B and Materials and Methods). This packing parameter shows a high correlation with the topological convergence (Fig. 6G), justifying its use as a proxy in this and subsequent developmental stages with more complex shapes. When the packing parameter is analyzed for ZP-less and control embryos, the correlation between the packing parameter and the topology is maintained in ZP-less embryos (Fig. 6H), and the evolution rate of the packing parameter over

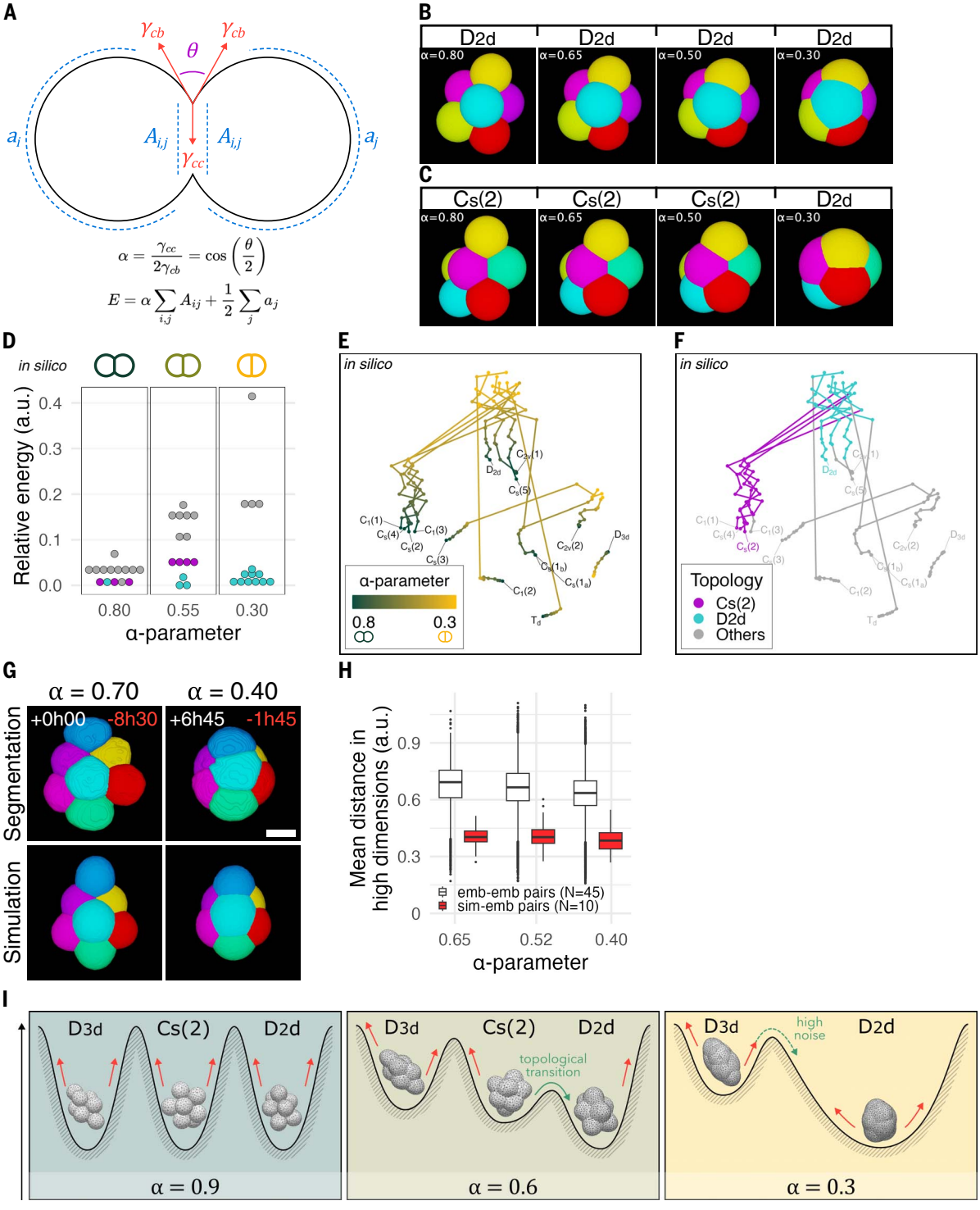

Fig. 4. Surface energy minimization with compaction is sufficient to recapitulate geometrical and topological convergence. (**A**) Diagram and equations of the biophysical model, the α-parameter (top) and the total energy of an embryo [(E) bottom]. Blue, cell-cell ($A_{i,j}$), and cell-medium (α_i) surface areas; red, cell-cell (γ_{cc}), and cell-medium (γ_{cb}) surface tensions; magenta, angle between the surface of two adjacent cells (θ). (**B**) and (**C**) In silico compaction of the D_{2d} (B) and $C_s(2)$ (C) packings from α = 0.8 to α = 0.3 showing a topological transition to D_{2d} at α = 0.3 in (C). (**D**) Relative energy after compaction of the initial 13 rigid packings, colored by their topological proximity to $C_s(2)$ (magenta), D_{2d} (cyan), and other rigid packings (gray). Color may differ from the initial packing as a result of topological transitions. (**E**) and (**F**) t-SNE projection of the morphomap of the 13 rigid packings during compaction. Each rigid packing is represented with a sequence of connected points from α = 0.8 to α = 0.3 and colored as a function of the compaction parameter (E) and the topological proximity to $C_s(2)$ (magenta), D_{2d} (cyan) and other rigid packings (gray) (F). Labels, the initial rigid packing at α = 0.8. (**G**) Visual comparison of an embryo (top row) and its simulation (bottom row) at the start (α = 0.7) and the end (α = 0.4) of the simulation. Time in hours after the start (white) and before the end (red) of the 8-cell stage. Scale bar, 25 μm. (**H**) Mean geometrical distance in-between embryos (white, "emb-emb") and between embryos and

simulations (red, "sim-emb") for α = 0.65, 0.52, and 0.4. N, number of pairs. (**I**) Schematic summary of the physical model. Uncompacted rigid packings (α = 0.9) are energetically equivalent and the noise is not high enough to escape from local minima (red arrows). Compaction (α = 0.6) biases the local minima relative energy and favors noise-induced topological transitions (solid green arrow). At high compaction (α = 0.3), many topologies transitioned to D_{2d}, although some topological transitions [from D_{3d}, $C_{2v}(2)$, $C_s(3)$ and $C_s(1a)$] require more noise (dashed green arrow) or a longer timescale. See also fig. S4, A and B.

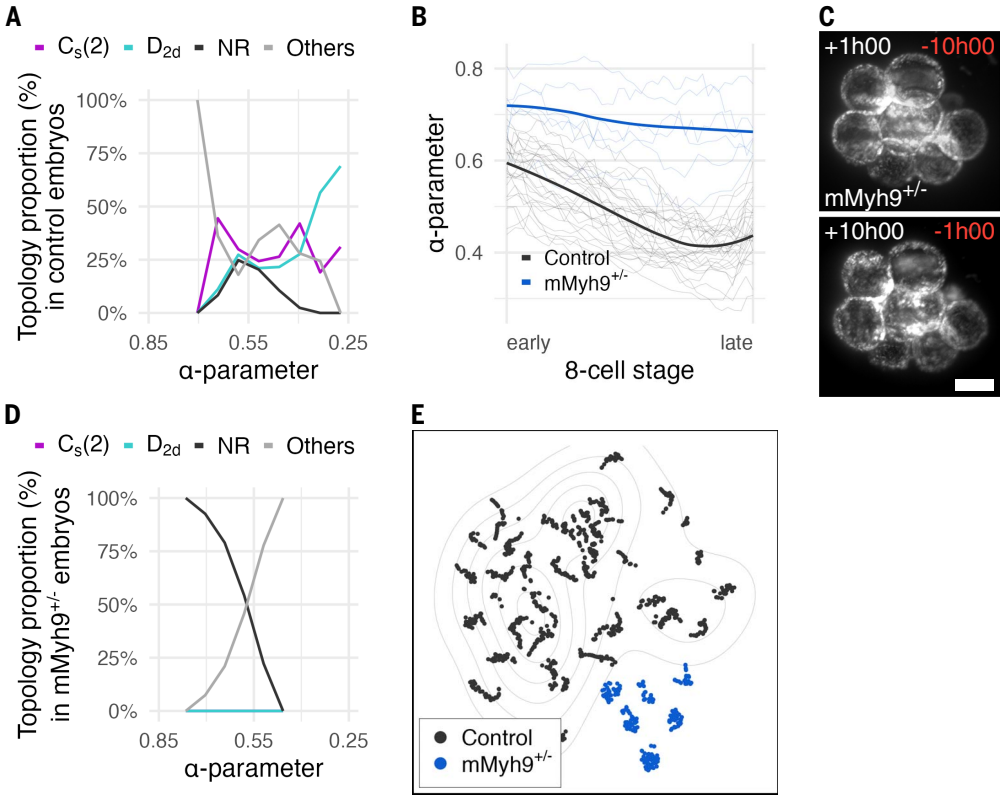

Fig. 5. Compaction and surface contractility drive topological transitions. (**A**) and (**D**) Proportion of $C_s(2)$ (magenta), D_{2d} (cyan), other rigid packings (others, gray), and NR packings (black) as a function of the compaction parameter in control mouse embryos [(A) *n* = 29 embryos] and mMyh9$^{+/-}$ mutants [(D) *n* = 6 embryos]. (**B**) Normalized time course through the 8-cell stage of the mean α-parameter for control mouse embryos (black, *n* = 29 embryos) and mMyh9$^{+/-}$ mutants (blue, *n* = 6 embryos). Light colors, individual tracks. See also fig. S5F. (**C**) Max projection of a representative live imaging of mMyh9$^{+/-}$ mutants at the beginning (top) and the end (bottom) of the 8-cell stage (*n* = 6 embryos). Time after the beginning (white) and before the end (red) of the 8-cell stage. Scale bar, 25 μm. See also movie S5. (**E**) t-SNE projection of the morphomap showing control mouse embryos (black, *n* = 29 embryos) and mMyh9$^{+/-}$ mutants (blue, *n* = 6 embryos). Isolines, density map at the end of the 8-cell stage of control embryos. See also fig. S5I.

time is identical between control and ZP-less embryos (Fig. 6I, same slope). Second and conversely, experimental reduction of the perivitelline space by crosslinking alginate sodium in the perivitelline space [see Materials and Methods and (*60*)] led to an overall increase of the packing parameter (Fig. 6J).

Together, these findings consistently suggest that the ZP restricts the initial space of potential configurations, constraining the embryo trajectories toward those leading to an optimal packing, in agreement with the lower number of different topologies in monkey 8-cell embryos (fig. S3C).

Variability in cleavage timing promotes robustness in morphogenesis and ICM-TE patterning

We have thus far characterized the temporal variability in cleavage timing and investigated the spatial convergence of the packings in the 8-cell embryo. Based on these findings, we next examined their impact on the forthcoming developmental stages, in particular on the first inside-outside cell fate patterning in the mouse embryo. First, we examined the impact of spatial convergence of the 8-cell embryo on the inside-outside cell segregation that happens in the 16-cell embryo. To determine the packing parameter at the 16-cell stage, we first defined an outer cell as one belonging to the group with higher contact-free surface area, of the two groups forming a bimodal distribution of the contact-free surface area (Fig. 7A, see also Materials and Methods). When the packing parameter of the 16-cell embryos was computed using outer cells, it showed a clear correlation with that of the 8-cell embryos [Pearson correlation $R = 0.659$ ($P < 0.01$), Fig. 7B] and the number of inner cells [Pearson correlation $R = 0.591$ ($P < 0.01$], Fig. 7C and fig. S7A], indicating that spatial convergence at the 8-cell stage may enhance the packing regularity, and hence the generation of inner cells in the 16-cell embryos. These findings suggest that spatial convergence and higher packing may result in a higher number of inner cells in the early mouse embryo.

Next, we investigated the impact of variability in cleavage timing on the spatial convergence and precision in embryo patterning. To test the impact of temporal variability, we synchronized mitotic entry at the 8- to 16-cell cleavage (Fig. 7D) using an inhibitor of the Anaphase-promoting Complex APC/C (APCin) or a blocker of microtubule polymerization (Nocadazole) during the 8- to 16-cell mitotic period (group "m-phase"), whereas control embryos underwent the same treatment during the intermitotic period and hence had no impact on division synchrony (group "interphase"). The APCin-treated embryos in the m-phase group had a significantly lower packing parameter at the 16-cell stage (mean ± s.d. = 0.29 ± 0.06) (Fig. 7, E and F) compared to the non-synchronized embryos in the interphase group (mean ± s.d. = 0.40 ± 0.11) and the untreated group (mean ± s.d. = 0.47 ± 0.18), while maintaining a high number of inner cells (fig. S7, B to D). Notably, a similar effect was obtained in ZP-less embryos with disrupted topologies (fig. S7E), suggesting a mechanistic link between synchronous divisions and topological disruption. Furthermore, mitosis synchronization resulted in a lower proportion of the ICM-fated Sox2$^+$ cells in the m-phase group

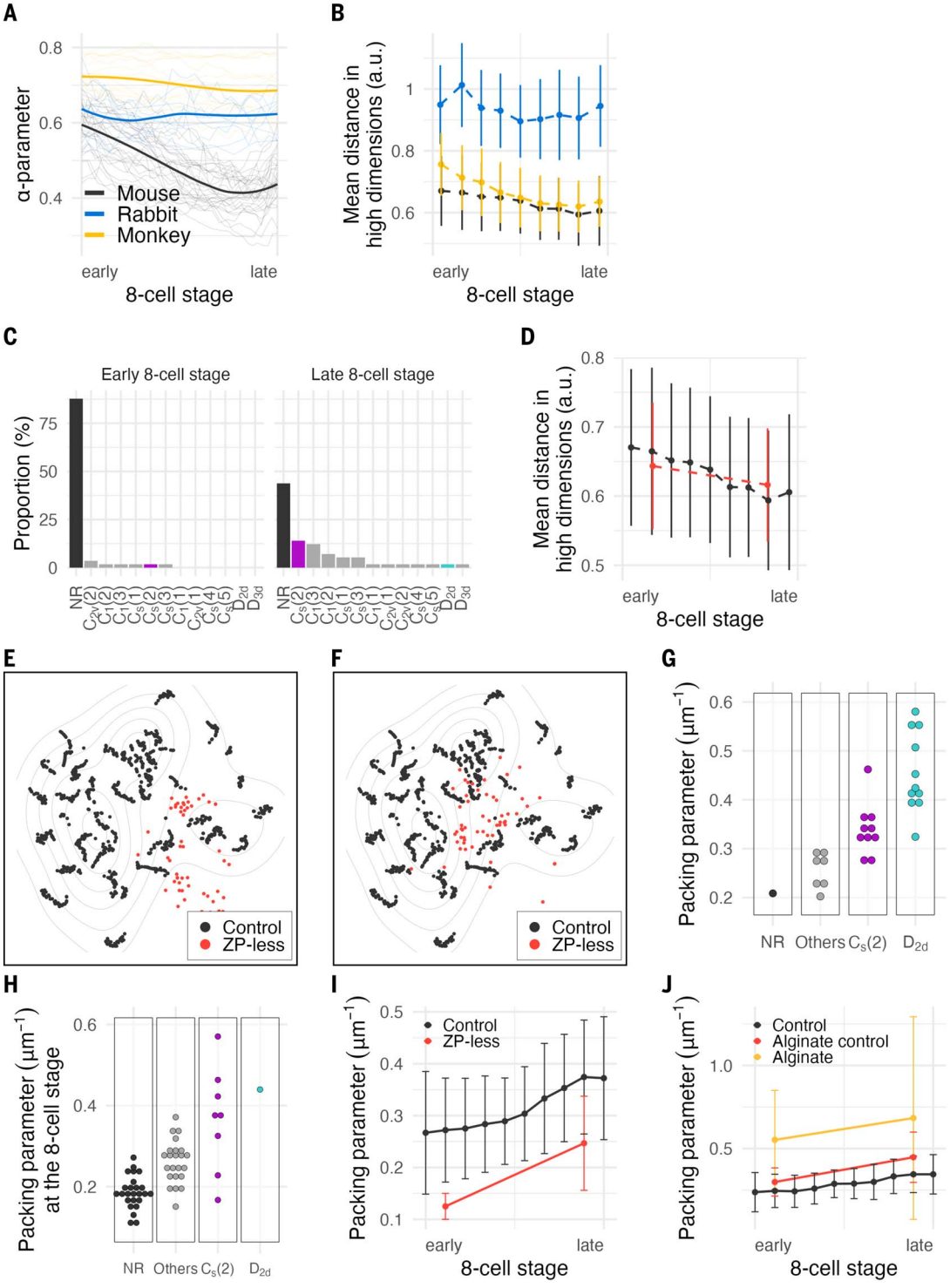

Fig. 6. ZP facilitates convergence by constraining the space of possibilities. (**A**) and (**B**) Normalized time course through the 8-cell stage of the mean compaction parameter α [(A) solid lines] and the mean distance in high dimensions [(B) dashed lines] in mouse embryos (black, *n* = 29), rabbit embryos (blue, *n* = 10), and monkey embryos (yellow, *n* = 12). Light color lines, individual embryo tracks. (**C**) Distribution of the proportion of $C_s(2)$ (magenta), D_{2d} (cyan), NR packings (black) or other minimally rigid packings (gray) identified in mouse embryos without ZP 1 hour and 30 min after the beginning (left) and the end (right) of the 8-cell stage (*n* = 57 embryos). See fig. S3C for comparison with embryos with ZP. (**D**), (**I**), and (**J**) Normalized time course through the 8-cell stage of the mean ± s.d. of the pair-wise geometrical distances (D) and the packing parameter (I) and (J) in control mouse embryos [black in (I) and (J), *n* = 29], mouse embryos without ZP [red in (I), *n* = 57], and mouse embryos incubated in alginate sodium without cross-linking [red in (J), *n* = 11], and with cross-linking [yellow in (J), *n* = 21]. (**E**) and (**F**) t-SNE projection of the morphomap with ZP-less embryos (red, *n* = 57) 1 hour and 30 min after the beginning (E) and before the end (F) of the 8-cell stage. Control embryos (black, *n* = 29) are also shown for reference. (**G**) and (**H**) Packing parameter at the end of the 8-cell stage as a function of the topology of the embryo with [(G), *n* = 20 embryos] and without [(H), *n* = 57, embryos] zona-pellucida.

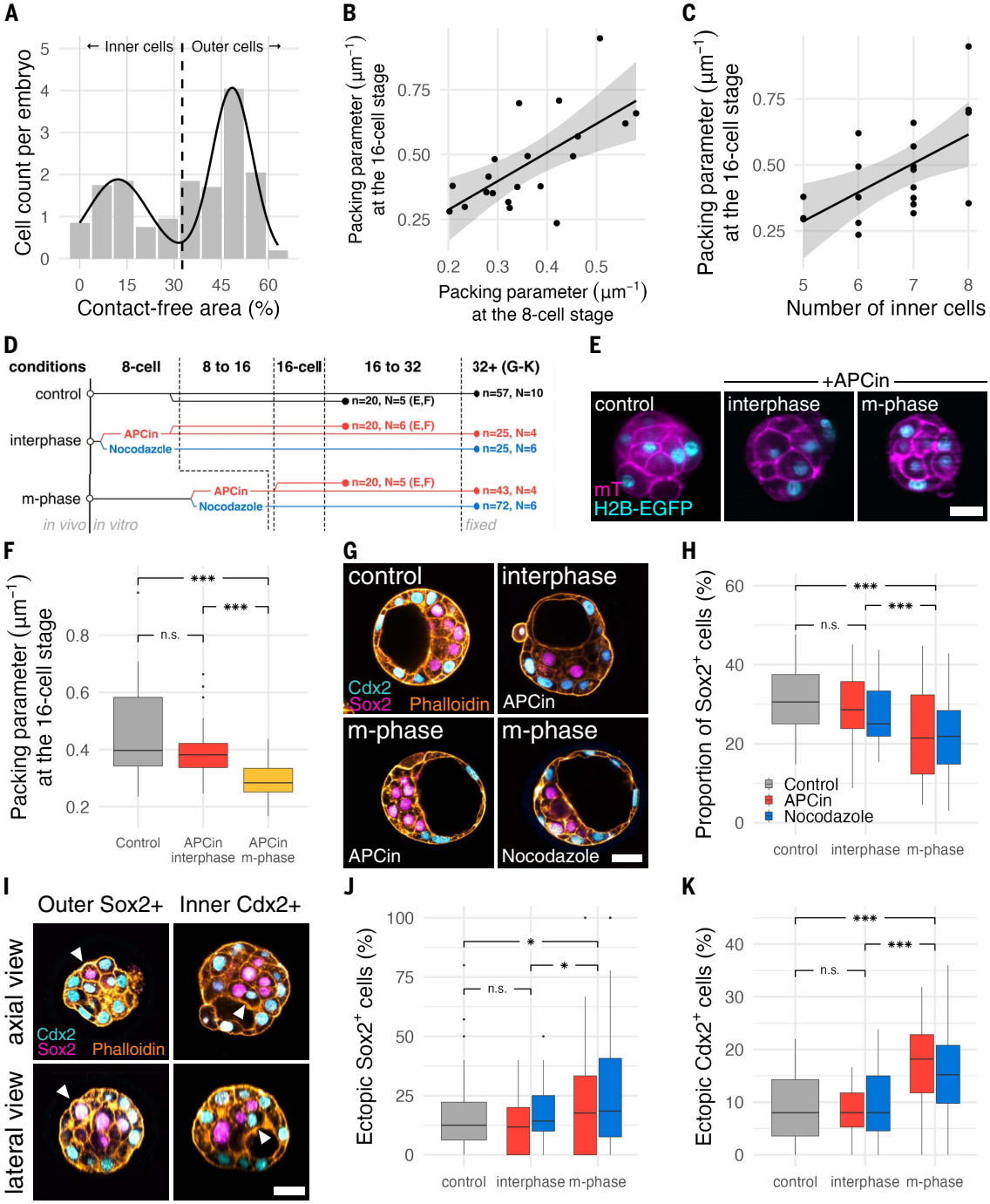

Fig. 7. Variability in cleavage timing promote robustness in morphogenesis and ICM-TE patterning. (**A**) Bimodal distribution of contact-free area of individual cells (gray bars, n = 320 cells from 20 embryos) fitted with inner and outer Gaussian distributions (black line, mean ± s.d. = 12.1% ± 9.6 and 48.4% ± 6.5). Dashed line, cutoff between inner and outer cells (32.6%). (**B**) and (**C**) Packing parameter two hours after the start of the 16-cell stage as a function of the packing parameter at the end of the 8-cell stage [(B) Pearson correlation R = 0.658 (P < 0.01)]. and the number of inner cells [(C) Pearson correlation R = 0.591 (P < 0.01)]. Solid line, linear regression. Shaded ribbon, standard error. (**D**) Diagram of the synchronization experiments done in (E) to (K). Embryos were either untreated (control) or treated with APCin (red) or Nocodazole (blue) at the beginning (group interphase) or end (group m-phase) of the 8-cell stage (see Materials and Methods). n, sample size; N, number of experiments. (**E**) Representative cross-section of live embryos at the 16-cell stage from groups control (left), interphase (middle) and m-phase (right). Magenta, mT (membranes); cyan, H2B-EGFP (chromatin). Scale bar, 25 µm. (**F**) Packing parameter two hours after the start of the 16-cell stage in control (gray), and APCin-treated groups interphase (red) and m-phase (orange). Two-sided Mann-Whitney test; n.s., non-significant; ***, P-value < 0.001. See (D) for sample size. (**G**) Representative cross-section of fixed embryos from group control (top-left), group interphase (top-right, APCin), and group m-phase (bottom row). Cyan, Cdx2 (TE-fated cells); magenta, Sox2 (ICM-fated cells); orange, phalloidin (F-actin). Scale bar, 25 µm. (**H**), (**J**), and (**K**) Box plot of the proportion of Sox2$^+$ cells (H), ectopic Sox2$^+$ cells (J) and ectopic Cdx2$^+$ cells (K) in embryos treated with APCin (red), Nocodazole (blue) or untreated (gray). Two-sided Mann-Whitney test; n.s., non-significant; *, P-value < 0.05; ***, P-value < 0.001. See (D) for sample size. (**I**) Axial (top) and lateral (bottom) cross-section of fixed embryos from group m-phase + APCin. Arrowhead indicates ectopic Sox2$^+$ (left) and Cdx2$^+$ (right) cells. Colors and scale bar as in (G).

at the 32-cell stage compared with the control groups, both after APCin or Nocodazole treatment (Fig. 7, G and H, and fig. S7F). This indicates that synchronization of the fourth cleavage led to formation of the lower proportion of ICM-fated cells in the embryo. Moreover, treated embryos showed significantly higher proportions of cells ectopically expressing Sox2 or Cdx2 (Fig. 7, I to K). Collectively, these results demonstrate that a certain degree of desynchronization of the cleavages in the early mouse embryo enhances embryo packing, generation of the ICM fate, and precision in the inside-outside patterning.

Concluding remarks

We measured and manipulated spatial and temporal variabilities in early mammalian embryogenesis, which demonstrated that spatial and temporal variabilities are functionally linked and an asynchrony in cell divisions facilitates robust morphogenesis and patterning.

Measurement and manipulation of temporal and spatial variabilities

Although cell lineage has been established for many species, few studies have focused on the cell-to-cell variability in spatial arrangement or cleavage timing (*19*, *32*, *33*, *61*–*67*). With a small number of cells and progressively accumulating variabilities in space and time, early mammalian embryos present an excellent opportunity to measure the building of variabilities during development.

To measure spatial variability we developed a morphological metric based on exponential splines and compared embryos geometrically. Unlike other methods (*44*, *68*–*76*), exponential splines encompass all geometrical hidden features (including volume, position, contacts, and compaction) with an arbitrary number of parameters and few assumptions, offering a generic tool to build morphomaps. Further, geometrical data are ultimately reduced to a few parameters that inherently approximate the actual cell shape. In spite of this approximation, we observed a high standard deviation in inter-embryonic distance, due to the high dimensions of the underlying space, while it displayed a highly significant decrease over time. We complemented the geometric analysis with a topological exploration of the possible cell packings of the embryo. This approach offers a theoretical framework that can add landmarks to morphomaps, enhancing their intuitive interpretability.

The spatial variability at the beginning of an intermitotic period may be largely influenced by previous cell divisions as cytokinesis generates force separating two daughter cells, rearranging embryonic packings abruptly, in a stochastic fashion. In the present study, experimental synchronization of the divisions revealed a functional link between temporal and spatial variabilities in embryogenesis; however, future studies may directly perturb the spatial arrangement of the cells.

It will also be interesting to examine whether temporal variability in cleavage timing can be predicted, for instance, by cell size, that reportedly has an impact on cell cycle dynamics (*77*). Overall, because spatiotemporal variability is widespread, it will be interesting to explore its possible source (*78*–*80*) and role in various developmental contexts.

Optimal spatiotemporal variability facilitates robust morphogenesis and patterning

We showed that cortical contractility drives topological transitions toward an optimally packed shape by lowering the surface energy. However, an infinite number of trajectories are possible. What makes the embryo follow one trajectory over another is yet to be elucidated and depends on the shape of the energy landscape, passive minimization of surface energy, and active cellular mechanisms generating fluctuating noise in the system. Additional mechanisms may constrain embryos to a limited subset of the morphomap, e.g., the possible spatial coupling between sister cells (*81*), or the geometrical constraint by the ZP, as with the eggshell in *Caenorhabditis elegans* (*82*).

We also showed that multiple sources of noise affect mammalian embryo development, including cleavage asynchrony and cell shape fluctuation. These variabilities at the cellular level influence the packing at the embryo level, and minimization of contractility driven surface energy buffers variability and explain geometric and topological convergences of the embryo. Notably, there are a number of local stable states in the system, meaning that some level of fluctuations is therefore required for transitions toward the global minimum. The idea that noise is not detrimental to reach a given stable state (*83*–*85*), but instead might be necessary to avoid being trapped in local minima, has been explored in computer science as well as in physics and chemistry (*86*–*89*). We thus conjecture that intermediate levels of variability—spatial or temporal, either arising from cleavages or contractility fluctuations—might be optimal for converging toward stereotypical embryo shapes and patterns.

Shared and distinct features across mammals highlight essential processes ensuring developmental robustness

Our analysis also demonstrated that the cellular morphogenesis of mouse, rabbit, and monkey embryos can be described in a shared morphomap, revealing a key similarity between mammalian species. Rabbit embryos show a higher spatial variability and a lower proportion of D_{2d} packing, in agreement with our model, given that compaction happens only from the 16- to the 64-cell stage (*90*, *91*). By contrast, monkey embryos display robust geometrical and topological patterns despite the lack of compaction at the 8-cell stage (*92*), where the ZP appears to exert higher spatial constraints (*43*, *82*). Alternatively, higher cleavage asynchrony may facilitate robust morphogenesis, by promoting an optimal packing from the early 8-cell stage.

Overall, the dynamics of the variability in cleavage timing is closely linked to the spatial organization of the cells within the embryo, and ultimately to morphogenesis and patterning. Our finding of species-specific dynamics of variability in cleavage timing suggests the possibility that the temporal variability may be an evolutionary trait generating an optimal spatial noise, ultimately ensuring robustness in embryogenesis.

Material and Methods

Mouse work

We performed mouse animal work in the Laboratory Animal Resources (LAR) at the European Molecular Biology Laboratory with permission from the Institutional Animal Care and Use Committee (IACUC) overseeing the operation (IACUC number TH11 00 11). LAR is operated as stated in international animal welfare rules (Federation for Laboratory Animal Science Associations guidelines and recommendations). Mouse colonies are maintained in specific pathogen-free conditions with 12 to 12 hours light-dark cycle. All mice used for experiments were older than 8 weeks.

Rabbit work

We performed rabbit animal work following the International Guidelines on Biomedical Research involving animals, as promulgated by the Society for the Study of Reproduction, and with the European Convention on Animal Experimentation. The researchers involved in work with the rabbits were all licensed for animal experimentation by the French veterinary services. The rabbit experimental design was carried out under the approval of national ethic committee (APAFIS #2180-2015112615371038v2) and under the approval of the local ethic committee (Comethea n°45, registered under n°12/107 and n°15/59).

Monkey work

We performed monkey animal work with female cynomolgus monkeys (*Macaca fascicularis*), of ages ranging from 6 to 11 years. The light-dark cycle was maintained as 12 to 12 hours of artificial lighting from 8 a.m. to 8 p.m. Each animal was fed 20 g/kg of body weight of commercial pellet monkey chow (CMK-1; CLEA Japan) in the morning, supplemented with 20 to 50 g of sweet potato in the afternoon. Water was available ad libitum. Temperature and humidity in the animal rooms were

maintained at 25 ± 2°C and 50 ± 5%, respectively. The animal experiments were appropriately performed by following the Animal Research: Reporting in Vivo Experiments (ARRIVE) guidelines developed by the National Centre for the Replacement, Refinement & Reduction of Animals in Research (NC3Rs), and also by following "The Act on Welfare and Management of Animals" from Ministry of the Environment, "Fundamental Guidelines for Proper Conduct of Animal Experiment and Related Activities in Academic Research Institutions" under the jurisdiction of the Ministry of Education, Culture, Sports, Science and Technology, and "Guidelines for Proper Conduct of Animal Experiments" from Science Council of Japan. All animal experimental procedures were approved by the Animal Care and Use Committee of Shiga University of Medical Science (approval number: 2021-10-4).

Mouse lines

The following mouse lines were used in this study: (C57BL/6xC3H) F1 for WT, mTmG (*Gt (ROSA) 26Sor*$^{tm4(ACTB-tdTomato,-EGFP)Luo}$) (*93*), CAG H2B-EGFP (*Tg(HIST1H2BB/EGFP)1Pa*) (*94*) and *Myh9*^{tm5RSad} (*95*). Double transgenic mTmG ; H2B-EGFP line was generated by breeding mTmG (homozygous or heterozygous) females with H2B-EGFP males. Transgenic mMyh9 ; mTmG ; H2B-EGFP embryos were generated by maternal deletion of Myosin-9 using ZP3-Cre (*Tg(Zp3-cre)93Knw*) mice (*96*) and *Myh9*^{tm5RSad} mice. Myh9$^{tm5RSad/tm5RSad}$; Zp3$^{Cre/+}$ mothers were bred with mTmG ; H2B-EGFP fathers. mG line was generated by maternal excision of the mT sequence using ZP3-Cre mice and mTmG mice. Genotyping was done using the following primers:

1. mTmG and mG lines: 250 b.p. (transgenic) and 330 b.p. (wild-type) PCR product size with primers oIMR7318 (CTCTGCTGCCTCCTGGCTTCT), oIMR7319 (CGAGGCGGATCACAAGCAATA) and oIMR7320 (TCAATGGGCGGGGGTCGTT),
2. CAG H2B-EGFP: 900 b.p. (transgenic) PCR product size with primers CAG-F (GGCTTCTGGCGTGTGACCGGC) and EXFP-R (GTCTTGTAGTTGCCGTCGTC); 324 b.p. (wild-type) PCR product size with primers oIMR7338 (CTAGGCCACAGAATTGAAAGATCT) and oIMR7339 (GTAGGTGGAAATTCTAGCATCATCC); PCR must be done separately,
3. *Myh9*^{tm5RSad}: 770 b.p. (transgenic) and 600 b.p. (wild-type) PCR product size with primers Myh 9F (ATGGGCAGGTTCTTATAAGG) and Myh 9R (GGGACACAGTGGAATCCCTT)
4. ZP3-Cre: 300 b.p. (transgenic) PCR product size with primers *cre upper* (TGCTGTTTCACTGGTTGTGCGGCG) and *cre lower* (TGCCTTCTCTACACCTGCGGTGCT).

Recovery of mouse embryos

Embryos were recovered from super-ovulated female mice. For superovulation, intraperitoneal injection of 5 international units (IU) of pregnant mare's serum gonadotropin (PMSG, Intervet, Intergonan) and following injection of 5-IU human chorionic gonadotropin (hCG; Intervet, Ovogest 1500) 48 hours later were performed. 4-cell stage embryos were recovered at E2.0 by inserting a needle in the ampulla and flushing the oviduct and the uterus with KSOMaa including HEPES (H-KSOMaa; Zenith Biotech, ZEHP-050). Recovered embryos were washed three times in drops of KSOMaa (Zenith Biotech, ZEKS-050) and then transferred into 10 μl drops of KSOMaa covered with mineral oil (Sigma-Aldrich, M8410). Embryos were maintained in an incubator (Thermo Fisher Scientific) at 37°C with 5% CO2.

Recovery of rabbit embryos

New Zealand White female rabbits (20 to 22 weeks old) were super-ovulated using 5 subcutaneous administrations of porcine follicle stimulating hormone (pFSH, Merial, Stimufol) for 3 days before mating: two doses of 5 μg on day 1 at 12 hours intervals, two doses of 10 μg on day 2 at 12 hours intervals, and one dose of 5 μg on day 3 followed 12 hours later by an intravenous administration of 30IU hCG (Intervet, Chorulon) at the time of mating (natural mating). Embryos were collected from oviducts and perfused with DPBS (Thermo Fisher Scientific, 14190) at 19 hours post-coitum (h.p.c.) to obtain embryos at 2 pronuclei stage. Embryos were maintained in 0.5mL of TCM199-HEPES (Biochrom, F0665) + 10% foetal bovine serum (FBS, Thermo Fisher Scientific, 10500) + 0.5% of penicillin/streptomycin (Thermo Fisher Scientific, 15140) in a 4-well dish (Nunc, 176740) until the microinjection.

Intracytoplasmic sperm injection (ICSI)

Monkey oocyte collection was performed as described previously (*97*). Briefly, two weeks after the subcutaneous injection of 0.9 mg of a gonadotropin-releasing hormone antagonist (Takeda Chemical Industries, Leuplin for Injection Kit), a micro-infusion pump (ALZET Osmotic Pumps, iPRECIO SMP-200) with 15 IU/kg human FSH (hFSH, Merck Biopharma, Gonal-f) was embedded subcutaneously under anesthesia and injected 7 μL/h for 10 days. After the hFSH treatment, 400 IU/kg human chorionic gonadotropin (hCG, Asuka Pharmaceutical, Gonatropin) was injected intramuscularly. Forty hours after the hCG treatment, oocytes were collected by follicular aspiration using a laparoscope (Machida Endoscope, LA-6500). Cumulus-oocyte complexes (COCs) were recovered in alpha modification of Eagle's medium (MP Biomedicals, 09103112-CF), containing 10% serum substitute supplement (Irvine Scientific, 99193). The COCs were stripped off cumulus cells with 0.5 mg/ml hyaluronidase (Sigma-Aldrich, H4272). ICSI was carried out on metaphase II (MII)-stage oocytes in mTALP +HEPES (*98*) with a micromanipulator. Fresh sperm were collected by electric stimulation of the penis with no anesthesia.

In vitro transcription

H2B-EGFP mRNA was transcribed from plasmid #1 pCS-H2B-EGFP (*99*) (Addgene, Plasmid #53744). To construct pCS2-myrTagRFP-T (plasmid #2), TagRFP-T fused with eight amino acids, GSSKSKPK, at the N terminus for myristoylation was amplified (primer set: 5′-GGATCCATGG GCAGCAGCAA GAGCAAGCCC AAGAGCGAGC TGATTAAG-3′ and 5′-CTCGAGTCAC TTGTGCCC-3′) and cloned into the BamHI-XhoI sites of pCS2+. To construct pcDNA3.1-membrane-tdTomato-T2A-H2B-GFP-poly(A83) (plasmid #3), an amplified PCR product from pCAG-TAG (Addgene, Plasmid #26771) was cloned into the KpnI-NotI sites of pcDNA3.1-H2B mCherry-poly(A83) (*100*). The vector #3 was linearized with XhoI and treated with 0.5% SDS, 0.2 mg/mL Proteinase K (Thermo-Fisher, QS0510) for 30 min at 50°C, purified with phenol-chloroform, and precipitated with ethanol.

Then, the purified vectors were used as a template for in vitro transcription. The mRNA from plasmid #1 and #2 was transcribed using the mMESSAGE mMACHINE SP6 Transcription Kit (Thermo Fisher Scientific, AM1340) and purified with the NucleoSpin RNA Clean-up XS kit (Macherey-Nagel, 740902). The mRNA from plasmid #3 was transcribed using the mMESSAGE mMACHINE T7 Transcription Kit (Thermo Fisher Scientific, AM1344) and purified with the MEGAclear Transcription Clean-Up Kit (Thermo Fisher Scientific, AM1908).

Microinjection of mRNAs

Rabbit zygotes were microinjected into the cytoplasm with a mRNA's mix of H2b-GFP (50 ng/μL final concentration) and myrTagRFP-T (150 ng/μL final concentration) in water. Microinjections were performed using a DIC inverted microscope (Olympus, IX71) equipped with micromanipulators (Eppendorf, TransferMan NK) and electronic microinjector (Eppendorf, femtojet injector). After microinjection, unlysed embryos were cultured during 2 to 3 hours in 40 μL micro drops of TCM199 (Sigma-Aldrich, M4530) + 10% foetal bovine serum (FBS, Thermo Fisher Scientific, 10500) + 0.5% penicillin/streptomycin (Thermo Fisher Scientific, 15140) under mineral oil (Sigma-Aldrich, M8410) at 38.5°C under 5% CO2.

For microinjection in monkey eggs, the mRNA was co-injected with sperm during ICSI. The sperm were washed in a drop of 300 ng/μL mRNA, and co-injected into the MII-stage oocytes. Following co-injection, embryos were cultured in monkey culture medium (CMRL 1066 Medium (Thermo Fisher Scientific, 21540026) supplemented with 20% FBS) at 38°C in 5% CO2 and 5% O2.

Transport of microinjected rabbit zygotes

Two to three hours after microinjection, 0.5 mL tubes were over-filled with M2 (Sigma-Aldrich, M7167) at 38.5°C to remove air bubbles. Tubes were placed into an insulated box (Polystyrene foam transport box) with the Velvet cooling elements (Velvet, SVE2) and antifreeze elements (Velvet, AF1) to maintain 8°C during transportation. The samples were sent from the collection site (Jouy-en-Josas, France) to the European Molecular Biology Laboratory (Heidelberg, Germany) via a regular courier service overnight (17 to 19 hours). Before reception of the embryos, rabbit culture medium (TCM199 (Sigma, M4530) + 10% FBS (Thermo Fisher Scientific, 10500) + 0.5% penicillin/streptomycin (Thermo Fisher Scientific, 15140)) was freshly prepared and stored at 38.5°C and 5% CO2 for at least an hour. Upon reception of the embryos, the temperature inside the box was checked (8°C), the embryos were transferred to a 4-well dish (Nunc, 176740) with M2 (Sigma, M7167) at room temperature for 5 min, washed four times in 40 μL drops of equilibrated and prewarmed rabbit culture medium, then transferred to 10 μL drops of equilibrated and prewarmed rabbit culture medium covered with mineral oil (Sigma, M8410). Embryos were maintained in an incubator (Thermo Fisher Scientific) at 38.5°C with 5% CO2 for one hour until the beginning of the imaging. Microinjected and noninjected embryos were kept at collection site for the duration of the experiment. Developmental timing was checked at regular intervals. Survival rate and blastocyst formation was assessed for transported and non-transported individuals. Embryos at imaging site were delayed by 18 hours compared to embryos kept at collection site, corresponding to the time spent at 8°C during transportation. No differences were observed in survival rate and blastocyst formation between the microinjected embryos at the imaging site and at the collection site, indicating no observable effects of transportation other that "pausing" the development.

Transport of microinjected monkey embryos

Forty-five hours after microinjection, 4-cell stage monkey embryos were transferred into 300 μL monkey culture medium (CMRL 1066 Medium supplemented with 20% FBS) covered with 1 mL mineral oil in a 1.5 mL tube. Tubes were placed into 38.5°C water in a vacuum bottle in an insulated box to maintain temperature during 1.5 hours of transportation from collection site (Shiga University of Medical Science, Japan) to the imaging site (Kyoto University, Japan). Upon arrival, embryos were washed three times with prewarmed monkey culture medium, then transferred to 10 μL drops of equilibrated and prewarmed monkey culture medium covered with mineral oil. Embryos were maintained in an incubator (PHCbi, MCO-170MUV) at 38°C with 5% CO2 and 5% O2 for one hour until the beginning of the imaging. Microinjected and noninjected embryos were kept at collection site for the duration of the experiment, and developmental timing was checked at regular interval. Monkey embryos showed no observable difference between the control embryos kept at collection site and the embryos imaged and cultured at imaging site.

Chemical treatments

For Myosin inhibition (Fig. 5), 4-cell stage embryos were washed and cultured in preequilibrated KSOMaa (Zenith Biotech, ZEKS-050) supplemented with DMSO (vehicle; Sigma-Aldrich, D2650) and *para*-aminoblebbistatin (10 μM; Optopharma, DR-Am-89) for 24 hours until the 16-cell stage. For the synchronization of cell mitoses at the fourth cleavage (Fig. 7), 8-cell stage embryos were randomly sorted into three groups. Embryos in the control group were washed and cultured for 4 hours in preequilibrated KSOMaa supplemented with 1:1000 DMSO. Embryos in the interphase group and m-phase group were washed and cultured for 4 hours in preequilibrated KSOMaa supplemented with APCin (100 μM; Tocris Bioscience, 5747) or Nocodazole (0.5 μM; Sigma-Aldrich, M1404). Treatment of embryos in the interphase group started at early 8-cell stage. Treatment of embryos in the m-phase group started at late 8-cell stage. Embryonic stage (early or late 8-cell stage) was determined by visual inspection of the overall degree of compaction of the embryos in the group with bright-field binocular microscope (Zeiss, Discovery.V8). Embryos from the interphase group were subsequently excluded from analysis if the 8- to 16-cell stage cleavage started less than 2 hours after washing the drug. A significant synchronization was observed in embryos from the m-phase group. Specifically, the 8- to 16-cell stage transition was reduced by 1.58 hours on average (mean ± sd of group interphase: 2.61 ± 0.98 hours, $n = 20$; mean ± sd of group m-phase: 1.03 ± 0.59 hours, $n = 20$), with the majority of the cells dividing in less than 15 min after washing. Only embryos having completed the 8- to 16-cell stage transition in 2 hours or less were included in the analysis.

Generation of heterochronic embryos

mTmG and mG mice were super-ovulated four hours apart. Embryos were recovered at the 4- to 8-cell stage and imaged every 30 min in the InVi-SPIM to identify the beginning of the 8-cell stage. Pairs of one mT and one mG expressing embryos with 3 to 6 hours of difference were selected to generate heterochronic chimeras. First, one of the two embryos was randomly chosen to be the donor. To dissociate the donor embryo into single blastomeres, the ZP was removed by incubating the embryos in pronase (0.5% w/v Proteinase K in H-KSOMaa supplemented with 0.5% PVP-40 (Sigma-Aldrich, P0930)) covered with mineral oil for 2-3 min. Embryos were then washed 5 times in 10 μL drops of H-KSOMaa. Afterwards, the embryos were placed into a 50 μL drop of dissociation medium (*101*) (KSOMaa without Ca^{2+} and Mg^{2+}). Blastomeres were then dissociated in the drop by pipetting up and down in a narrow glass capillary (Brand, 708744). Dissociated blastomeres were incubated in KSOMaa drops covered with mineral oil until the host embryo was ready for the graft. To prepare the host, we used a micromanipulation device (Narishige, MON202-D) mounted on a Zeiss Axio Observer Z1 microscope to create a slit in the ZP. First, the host embryos were placed in a 50 μL drop of H-KSOMaa covered with mineral oil in a glass-bottom dish (MatTek, P50G-1.5-14-F) and mounted on the microscope with temperature of the incubation chamber maintained at 37°C. To make a slit in the ZP of the host, a holding pipette and a pulled glass needle mounted on the micromanipulator were used. Both the holding pipette and pulled needle were custom-made from glass capillaries (Warner Instrument, GC100T-15) using a micropipette puller (Sutter Instrument, P-1000) and a microforge (Narishige, MF-900). The host embryo was maintained in place with the holding pipette and the glass needle was inserted tangentially to the embryo under the ZP and pulled in a perpendicular direction without damaging the cells, thus generating a slit in the ZP. Next, one of the donor's blastomeres was randomly picked and inserted in the slit under the host's ZP using another custom-made glass pipette mounted on the micromanipulator. The resulting 9-cell heterochronic chimeras were then transferred to KSOMaa and put back in the InVi-SPIM and imaged every half an hour until the 32-cell stage. Finally, timing of division was manually inspected from 8- to 16-cell stage and from 16- to 32-cell stage. Host and donor cells were identified based on the expression of mT or mG.

ZP dissection

Embryos were dissected out of their ZP at the 4-cell stage using a holding pipette and a glass needle (*102*). The holding pipette and needle were custom-made from glass capillaries (Warner Instrument, G100TF-6) pulled using a micropipette puller (Sutter Instrument, P-1000). To forge the holding pipette, the glass needle was cut to approximatively 80 μm diameter using a microforge (Narishige, MF-900) and the tip was fire-polished to approximatively 10 μm inner diameter. To forge the needle, the tip was melted onto the glass bead and pulled back to obtain a solid pointed tip. Both needle and pipette were bent to a 30° to 45° angle to be parallel to the dish surface when mounted on a micromanipulator (Narishige, MON202-D). The

holding pipette was used to apply controlled pressures using mineral oil-filled tubing coupled to a piston of which the position was moved using a microscale translating stage (Narishige, IM-9B).

Gelation of the perivitelline space

Embryos recovered at the 1-cell stage were incubated for 90 min in warm H-KSOMaa medium containing 1% of alginic acid sodium salt (Sigma-Aldrich, A1112). They were rinsed briefly in H-KSOMaa and incubated for 30 min in H-KSOMaa (group alginate control) or in H-KSOMaa + 0.1% NaCl + 0.13% $CaCl_2$ (group alginate). Following gelation, embryos were rinsed in preequilibrated KSOMaa and cultured at 37°C and 5% CO_2 until the beginning of imaging at 4-cell stage.

Immunostaining

Embryos were fixed in 100µL of 4% paraformaldehyde (PFA, Electron Microscopy Sciences, 19208) in DPBS for 15 min at room temperature, washed three times for 5 min in DPBS with 0.1% Tween-20 (wDPBS, Sigma-Aldrich, P7949) + 1% bovine serum albumin (BSA, Sigma-Aldrich, 9647), permeabilized 15 min at room temperature in DPBS with 0.5% TritonX-100 (Sigma-Aldrich, T8787), washed three times for 5 min in wDPBS+1% BSA, and blocked 4 hours at room temperature in wDPBS+3% BSA. Embryos were then transferred into 70 µL of primary antibody solution in wDPBS+3% BSA and incubated overnight at 4°C. Primary antibodies against Cdx2 (Biogenex, MU392A-UC) and Sox2 (Cell Signaling, D9B8N) were diluted at 1:150. Embryos were then washed three times for 5 min in wDPSB+1% BSA and transferred into 70 µL of secondary antibody solution in wDPSB+1% BSA supplemented with Phalloidin-Rhodamin (Thermo Fisher Scientific, R415) at 1:200 for 2 hours at room temperature. Secondary antibodies conjugated with Cy5 against mouse Ig (Jackson ImmunoResearch, 715-175-150) and Alexa Fluor 488 Plus against rabbit Ig (Thermo Fisher Scientific, A11008) were diluted at 1:200. Before imaging, embryos were washed three times for 5 min in wDPBS+1% BSA, transferred 10 min at room temperature in wDPBS+1% BSA supplemented with DAPI (1:1000, Thermo Fisher Scientific, D3751) to stain DNA, washed three times for 5 min in wDPBS+1%BSA and mounted in 5 µL drops of wDPBS for imaging the same day.

Confocal microscopy

Imaging of immunostained embryos was performed with LSM 780 (Zeiss). C-Apochromat 403 1.1 NA water objective (Zeiss) was used.

Light-sheet microscopy

Embryos were live-imaged using InVi-SPIM (Luxendo). Embryos were aligned in a V-shaped sample holder covered with transparent fluorinated ethylene propylene foil (FEP, Luxendo), in approximately 100 µL of culture medium covered with 200 µL of mineral oil to prevent evaporation. The sample holder was enclosed in an environmentally controlled incubation box with 5% CO2 and 5% O2 at 37°C (mouse), 38°C (monkey) or 38.5°C (rabbit). For Fig. 1, embryos were isolated in wells to facilitate their identification after imaging, fixation and immunostaining. To shape the wells, we used a flamed glass capillary (Marienfeld Superior, 2930210) with a spherical tip of approximatively 200 µm of diameter to carefully press and stretch the FEP foil shaping up to 50 wells per sample holder. InVi-SPIM was equipped with a Nikon 25x/1.1NA water immersion detective objective and a Nikon 10x/0.3 NA water immersion illumination objective. The illumination plane and focal plane were aligned before each imaging session and maintained during the imaging. Images were taken by a CMOS camera (Hamamatsu, ORCA Flash4.0 V2) using software LuxControl (Luxendo). The lasers and filters used were 488 nm with BP525/50 and 561 nm with LP561 to image GFP and tdTomato/RFP fluorophores respectively. Exposure time for each plane was set to 30 ms. Imaging was done using a lateral resolution of 0.104 µm/px or 0.208 µm/px binned to 0.416 µm for analysis. Due to technical difficulties with the motorized stage, the InVi-SPIM used a larger than requested step size between optical slices. To determine the real step size, we computed for each embryo the width:depth ratio and the height:depth ratio in voxels of all cells at every time point of the segmented 8-cell stage. Assuming that these ratio equals 1 on average, as with the width:height ratio, we determined the real step size in µm for each embryo individually (see table S1). Imaging settings, including duration of imaging and time interval for each dataset, are summarized in table S1.

Generation of cluster of spheres in silico

We describe the method to generate in silico surrogates of packings such that they can be manipulated using the software Surface Evolver (*54*), a classical tool to study the surfaces and topological transitions shaped by surface tension. Input data provides the geolocation of the center of masses of cells, area of contact between cells and volume of each cell. Output data are a file compatible with Surface Evolver (file extension *fe*). For each cell, we created a cloud of points at distance R of its center of mass, such that the enclosed volume corresponded to volume of the cell. For adjacent cells, we created a triangle—a simplex—that was shared among the two cells in contact. Then, we created the convex hull of the cloud of points, including the contact simplices if present, even though they can break locally the convexity of the object. This resulted in a structure made of triangular simplices to which we provided a consistent orientation such that they can be properly interpreted by Surface Evolver. Volumes were also given consistently with the volumes in the input data. The first optimization steps of Surface Evolver are sufficient to generate a structure akin to the input data, both at the topological and geometrical level, and also to remove the potential non-convex regions generated at the contact points. The surface tensions can then be modified such that one reproduces the compaction process. See also fig. S4F for a schematic description of the process.

In silico compaction and energy minimization

Following previous findings that cell-cell adhesion during mouse compaction could be described well by the analogy to soap bubble (*35*, *40*), the energy of a given configuration is defined by

$$E_{tot} = \sum_{i=1}^{8} \left(\gamma_{cf} A_{cf}^{i} + \frac{1}{2} \gamma_{cc} A_{cc}^{i} \right)$$

where we have summed by all eight cells their cell-fluid energy (γ_{cf} being the cell-fluid tension and A_{cf}^{i} the cell-fluid aa of cell i) and their cell-cl energy (γ_{cc} being t cell-cell tension and A_{cc}^{i} the area of cell i in contact with other cells, note that the factor $\frac{1}{2}$ is to avoid double summation). We set all cellular volumes to unity. We can set $\gamma_{cc} = 1$ without loss of generality, so that the minimization problem depends only on the tension ratio $\alpha = \frac{\gamma_{cc}}{2\gamma_{cf}}$. It has been shown previously that this parameter α can be estimated from the angles between cell-cell contacts and the fluid interface (Young-Dupré equation, see also Fig. 4A and fig. S2G). Note that $\alpha = \frac{1}{2}$ corresponds to soap bubbles (all tensions are equal and all angles are 120°), $\alpha = 0$ corresponds to only cell-fluid tension so that the embryo will be perfectly spherical regardless of the contact topology, and $\alpha > 1$ corresponds to the non-adhesive case as it becomes energetically favorable for cells to dissociate (as cell-cell tensions are larger than cell-fluid tensions).

To explore how each of the 13 rigid packings evolve with compaction, we first initialized the software with the 13 possible packings and a very small adhesion strength ($\alpha = 0.95$), which ensured that cells showed very small cell-cell contacts, and no tricellular junctions, in analogy with adhesive hard colloids (*47*). We then slowly decremented α by 0.05, each time allowing for equilibration to a minimal energy configuration. This allowed us to calculate how energies of each configuration evolve as a function of α. Importantly, while for α close to 1, energies of all 13 packings were very similar, as expected theoretically, decreasing α broke the degeneracy of the system. The local stability of these energy minima was verified in Surface Evolver

by coarsening and remeshing the surface, effectively adding noise and checking whether the system always converged toward the same energy configuration.

Nearest neighbor algorithm

For cell tracking, registration or alignment of two sets of 3D points (P_A and P_B) or 3D segmentation (S_A and S_B), we developed a nearest neighbor algorithm in Python, available in the package morphomap (see section Code availability). For segmentation, the center of mass of each cell in S_A and S_B was used to generate P_A and P_B respectively. First, we computed C_A and C_B, the centers of mass of P_A and P_B respectively. Second, P_A and P_B were translated to the origin such that $P_{A0} = P_A\text{-}C_A$ and $P_{B0} = P_B\text{-}C_B$. Third, we generated 125,000 transformation matrices including rotation (10 values between 0° and 360° for pitch, roll and yaw) and scaling (5 values 0.5, 0.75, 1.0, 1.25, and 1.50 along the X, Y, and Z axis), corresponding to 125,000 transformations tP_{B0} of P_{B0}. Pairwise Euclidean distances between points of tP_{B0} and P_{A0} were computed and sorted. The pair were assigned once, in order from the smallest distance to the biggest distance. If tP_{B0} had unassigned cells after the first round, a second round of assignation was done, assuming mitosis. The alignment score was computed as the sum of the squared distance between assigned points of P_{A0} and tP_{B0}. The best three scores were kept and a new set of 125,000 transformation matrices was generated exploring the grid cell around the selected values, progressively refining a grid search of rotations and scaling. The algorithm stopped after 3 iterations (corresponding to variations of 0.36° for the rotation and 0.025% for the scaling). In case of segmentation, the score was weighted by the Jaccard index between segmented cells (number of voxels in common divided by the total number of voxels). The nearest neighbor algorithm produced a translation vector, rotation parameters, scaling parameters, and a list of cell assignment. Computation was distributed on the EMBL's cluster.

Tracking and manual curation

For mouse embryos, nuclear centers were detected using a Difference of Gaussians algorithm (*103*) (DoG). The best parameters for the DoG algorithm were found by a grid-search procedure which explored thousands of different configuration parameters simultaneously using EMBL's computing cluster. The best output was manually chosen and used for tracking using our nearest neighbor algorithm. Manual curation from the 4-cell stage to the 32- or 64-cell stage was performed by one operator using the software Mov-IT (*103*) and validated by a second operator. Alternatively, for rabbit and monkey embryos, we used a custom-made cell detection and tracking algorithm (unpublished) based on nuclear segmentation with Cellpose (*104*, *105*) and semi-automatic shape tracking using Napari (*106*). All the cells were inspected. We excluded from analysis all embryos showing sign of aneuploidy based on nuclear signal (fragmented nuclei, micro-nuclei and lagging chromosomes) and membrane signal (abnormal cytokinesis).

Identification of cell fate and back-tracking

Identification of inner-cell-mass (ICM) and trophectoderm (TE) progenitor cells was done by fixation and immunostaining of embryos less than 15 min after the end of the live imaging. Sox2 and Cdx2 positive cells (respectively ICM- and TE-fated cells) were identified by the signal intensity and mapped on the last time point of the live-imaged dataset. The alignment of the cells from the confocal imaging of immunostained embryos and the cells from the corresponding live-imaged embryos was done using our nearest neighbor algorithm. The identity of cells as determined by the immunostaining was then transferred to the last time point of the live-imaged dataset. Finally, cell identity was propagated backward with a higher priority to TE-fated cells.

Measurement of cleavage timing variability

Cells were annotated with their generation number determined by the number of cells at the beginning of the imaging (zygote stage being the first generation). After each mitosis, daughter cells' generation was incremented. The variability in division timing at the n^{th} cleavage was measured as the standard deviation of the timing of division (in hours) of the cells of the n^{th} generation in one embryo. When multiple embryos were pooled, the timing of division at one generation was first centered to zero for each embryo before extracting the standard deviation from the fitting of a Gaussian distribution to the pooled cells at that generation. Because fitting with a Gaussian distribution predicts unreliable standard deviation if more than 30% of the data are missing from one side of the curve, embryos with less than 80% of cells dividing to the n^{th} generation during the imaging period were removed from the analysis.

Time and spatial difference between cells

For each embryo, all unique pair of cells of the same generation were generated. The time difference was measured as the time (in hour) between the divisions of the cells in the pair. The spatial difference was measured as the Euclidean distance between the two cells 15 min before the first of the two mitoses.

Normalization by cell cycle length

Embryos of different species may have significantly different cell cycle length (approximately 20 hours in early monkey, compared to 11 hours for mouse and rabbit embryos). To minimize the impact that such difference may have on the measured timing of division, we normalized the variance by the average cell cycle length of the previous generation, if possible. Because the imaging period often started during the 4-cell stage in mouse, we normalized the variability of the division timing during the third cleavage (4- to 8-cell stage) by the average cell cycle length of the 8-cell stage instead.

Membrane segmentation and curation

The segmentation pipeline used to process the 3D images of the membrane signal uses the PlantSeg package (*107*) based on previous work done in electron microscopy images of neural tissue (*108*–*110*) where a combination of a strong boundary predictor and graph partitioning methods has been shown to deliver accurate segmentation results. Briefly, the method consists of two major steps. In the first step, a convolutional neural network (CNN) is trained to predict cell boundaries. Then, a region adjacency graph is constructed from the pixels with edge weights computed from the boundary predictions. In the second step, a partitioning of the region adjacency graph is computed to produce the segmentation. The accuracy of this method is highly dependent on the boundary segmentation given by the CNN. Since no ground truth segmentation was initially available for our data, no dedicated CNN could be trained to accurately segment cell membranes. Instead, we used the following iterative procedure. In the first iteration a pretrained CNN available in the PlantSeg package was used to generate the initial membrane probability maps. Specifically, we used a CNN trained on the confocal stacks of the *Arabidopsis* ovules dataset named "*confocal_unet_bce_dice_ds2*". Having the cell boundary prediction, the initial segmentation was produced with PlantSeg. Then, the segmentation has been improved by visually choosing the most correctly segmented regions, manually correcting the remaining errors and using the results as training data for a dedicated neural network for the membrane prediction task. This process of choosing the best segmentation, proofreading, and re-training the network was performed three times. A fourth optimization was performed individually for each dataset, using five time points regularly spaced in the time series and manually curated to generate a dedicated neural network for the membrane prediction of a unique dataset, allowing for the segmentation of hundreds of time points with almost no curation required.

The resulting network was used as a basis for the graph partitioning in PlantSeg. For the final segmentation of embryos into cells we have chosen the MultiCut graph partitioning strategy (*111*–*113*), implemented (*114*) in PlantSeg. The best hyperparameters for the MultiCut

algorithm have been found by a grid-search procedure which explored thousands of different configuration parameters simultaneously using EMBL's computing cluster. Manual curation and editing were performed by one operator using a custom-made application (unpublished) and validated by a second operator.

Preparation of the labeled data for analysis

After curation, the segmentation data were scaled without interpolation with Fiji (*115*) to generate isotropic voxel size of 0.416 × 0.416 × 0.416 μm^3. Polar bodies were automatically removed from the segmentation file based on volume size and blastomeres were automatically tracked using our weighted nearest neighbor algorithm. Finally, segmentation holes and gaps between cells were closed with a dilation of one voxel around each labeled cell. For each embryo, we checked sudden changes of cell volume and Jaccard index over time to identify and correct potential segmentation errors.

Parametrization with exponential splines

Each cell has been parametrized independently using exponential splines. Assuming a continuous surface without holes, cells are modeled as deformations of a continuously defined parametric spline sphere with n longitudes and m latitudes. In this study, we used $n = 5$ and $m = 5$ to maximize the accuracy of the geometrical approximation while avoiding overfitting of artefactual information (e.g., voxel aliasing). Equations have been re-derived from previous work (*39*) to accommodate for mathematical errors. The Python package splinefit is available as part of the package morphomap (see section Code availability).

Setup

Data are assumed to be 3D image volumes (in TIFF format) containing integer masks for each individual cells. Each cell is a single connected component which voxels are all labeled with the same integer value. Label values may be any unique integer, and background voxels are labeled as 0.

Fitting pipeline

Cells are assumed to have a sphere topology (no void, no hole). We therefore model them as deformations of a continuously defined parametric spline sphere. The resulting closed surfaces are C^2 smooth. We advocate for a continuously defined parametric (implicit) representation as it allows for fast surface comparison across physical object size and voxel size. In this pipeline, each cell is processed independently. The embryo is thus defined as a collection of non-interacting deformed spheroids with no built-in notion of contact or spatial interactions.

Parametrization, general form

The sphere σ of radius $r \in \mathbb{R}$, embedded in $\mathbb{R}^3$, is defined in its parametric form for $s, t \in [0,1]$ as

$$\sigma(s,t) = \begin{pmatrix} r\cos(2\pi t)\sin(\pi s) \\ r\sin(2\pi t)\sin(\pi s) \\ r\cos(\pi s) \end{pmatrix}.$$

The two parameters, t and s, run along the latitude and longitudes respectively, as depicted in fig. S2A. Note that latitudes are defined as full circles (closed), while longitudes are half-circle arcs (open). The parametric form of a 3D ellipsoid naturally follows for $s, t \in [0,1]$ as

$$\eta(s,t) = \begin{pmatrix} a\cos(2\pi t)\sin(\pi s) \\ b\sin(2\pi t)\sin(\pi s) \\ c\cos(\pi s) \end{pmatrix},$$

with $a, b, c \in \mathbb{R}$ as the three ellipse axes.

Parametrization, spline model

The 3D ellipsoid η can be perfectly interpolated as a spline surface following

$$\eta(s,t) = \sum_{l=-1}^{M_s} \sum_{k=0}^{M_t-1} c[l,k]\,\varphi_{\frac{2\pi}{M_t},per}(M_t t - k)\,\varphi_{\frac{\pi}{M_s-1}}((M_s-1)s - l) \quad (1)$$

where $c[k,l]$ are the parameters of the model, called control points. The integers M_t and M_s correspond to the number of parameters along each latitude and longitude, respectively. The function φ_α: $\mathbb{R} \to \mathbb{R}$ is the exponential spline basis (*116*), given by

$$\varphi_a(x) \begin{cases} \dfrac{\cos(\alpha|x|)\cos\left(\frac{\alpha}{2}\right) - \cos(\alpha)}{(1-\cos(\alpha))} & 0 \le |x| < \frac{1}{2} \\ \dfrac{\left(1 - \cos\left(\alpha\left(\frac{3}{2} - |x|\right)\right)\right)}{2(1-\cos(\alpha))} & \frac{1}{2} \le |x| < \frac{3}{2} \\ 0 & \frac{3}{2} \le |x| \end{cases} \quad (2)$$

The basis φ_α reproduces the space generated by $\{1, x, e^{j\alpha}, e^{-j\alpha}\}$. Because latitudes are closed circles, the basis associated to t is M_t-periodized as $\varphi_{\frac{2\pi}{M_t},per}(t) = \sum_{n\in\mathbb{Z}} \varphi_{\frac{2\pi}{M_t}}(t - M_t n)$.

The expression (1) is here normalized such that the two continuous parameters run in $[0,1]$.

For the ellipsoid to be properly closed, smoothness must be ensured at the poles. This translates to the two following conditions:

Interpolation, i.e., all longitudes meet at two well-defined points, the north pole c_N and the south pole c_S:

$$c_N = c[1,k]\,\varphi_{\frac{\pi}{M_s-1}}(-1) + c[0,k]\,\varphi_{\frac{\pi}{M_s-1}}(0) + c[-1,k]\,\varphi_{\frac{\pi}{M_s-1}}(1) \quad (3)$$

$$c_S = c[M_s,k]\,\varphi_{\frac{\pi}{M_s-1}}(-1) + c[M_s-1,k]\,\varphi_{\frac{\pi}{M_s-1}}(0) + c[M_s-2,k]\,\varphi_{\frac{\pi}{M_s-1}}(1) \quad (4)$$

Smoothness, i.e., each pole has a properly defined tangent plane characterized by two tangent plane vectors:

$$\frac{\partial\eta}{\partial s}(s,t)|_{s=0} = T_{1,N}\cos(2\pi t) + T_{2,N}\sin(2\pi t),$$

$$\frac{\partial\eta}{\partial s}(s,t)|_{s=1} = T_{1,S}\cos(2\pi t) + T_{2,S}\sin(2\pi t),$$

with $T_{1,N}, T_{2,N}, T_{1,S}, T_{2,S} \in \mathbb{R}^3$ the tangent plane vectors of the north and south pole, respectively. From (1), the above relations translate to

$$T_{1,N}\cos(2\pi t) + T_{2,N}\sin(2\pi t) = T_{1,N}(M_s-1)\sum_{l=-1}^{M_s}\sum_{k=0}^{M_t-1} c[l,k]\,\varphi_{\frac{2\pi}{M_t},per}(M_t t - k)\,\varphi'_{\frac{\pi}{M_s-1}}(-l) \quad (5)$$

$$T_{1,S}\cos(2\pi t) + T_{2,S}\sin(2\pi t) = T_{1,S}(M_s-1)\sum_{l=-1}^{M_s}\sum_{k=0}^{M_t-1} c[l,k]\,\varphi_{\frac{2\pi}{M_t},per}(M_t t - k)\,\varphi'_{\frac{\pi}{M_s-1}}((M_s-1) - l)$$

The initial set of control points parameterizing an ellipse of axes $a, b, c \in \mathbb{R}$ and center $p_0 \in \mathbb{R}^3$, with the north-south axis aligned along z, are given by

$$c_N = p_0 + \begin{pmatrix} 0 \\ 0 \\ c \end{pmatrix},\ c_S = p_0 - \begin{pmatrix} 0 \\ 0 \\ c \end{pmatrix},$$

$$T_{1,N} = \begin{pmatrix} a\pi \\ 0 \\ 0 \end{pmatrix},\quad T_{2,N} = \begin{pmatrix} 0 \\ b\pi \\ 0 \end{pmatrix},$$

$$T_{1,S} = \begin{pmatrix} a\pi \\ 0 \\ 0 \end{pmatrix},\quad T_{2,S} = \begin{pmatrix} 0 \\ b\pi \\ 0 \end{pmatrix},$$

and

$$c[l,k] = p_0 + \begin{pmatrix} aC_{\frac{2\pi}{M_t}}\cos\left(\frac{2\pi k}{M_t}\right)C_{\frac{\pi}{M_s-1}}\sin\left(\frac{\pi l}{(M_s-1)}\right) \\ bC_{\frac{2\pi}{M_t}}\sin\left(\frac{2\pi k}{M_t}\right)C_{\frac{\pi}{M_s-1}}\sin\left(\frac{\pi l}{(M_s-1)}\right) \\ cC_{\frac{\pi}{(M_s-1)}}\cos\left(\frac{\pi l}{(M_s-1)}\right) \end{pmatrix}$$

for l=1,..., M_s−2 and k=0,..., M_t−1, with

$$C_\alpha = \frac{2\left(1-\cos\left(\frac{2\pi}{\alpha}\right)\right)}{\cos\left(\frac{\pi}{\alpha}\right) - \cos\left(\frac{3\pi}{\alpha}\right)}$$

The surface (1) is thus fully determined by $M_t(M_s-2)+6$ parameters: c_N, c_S, $T_{1,N}$, $T_{2,N}$, $T_{1,S}$, $T_{2,S}$, and $c[l,k]$ for l = 1,..., M_s − 2, k = 0,... M_t − 1 (see also fig. S2B). Due to the support size of the exponential spline basis, extra control points are added at the extremities of each open longitude to ensure a correct behavior at the

boundaries. The extra control points c[*l*,*k*] for $l = -1, 0, M_s - 1, M_s$, $k = 0,\ldots M_t - 1$ are computed from the known parameters as

$$c[-1,k] = c[1,k] - \frac{T_{1,N}c_{M_t}[k] + T_{2,N}s_{M_t}[k]}{(M_s-1)\varphi'_{\frac{\pi}{M_s-1}}(1)} \tag{6}$$

$$c[0,k] = \frac{c_N - \varphi_{\frac{\pi}{M_s-1}}(1)(c[-1,k]+c[1,k])}{\varphi_{\frac{\pi}{M_s-1}}(0)} \tag{7}$$

$$c[M_s,k] = c[M_s-2,k] - \frac{T_{1,S}c_{M_t}[k] + T_{2,S}s_{M_t}[k]}{(M_s-1)\varphi'_{\frac{\pi}{M_s-1}}(1)} \tag{8}$$

$$c[M_s-1,k] = \frac{c_S - \varphi_{\frac{\pi}{M_s-1}}(1)(c[M_s-2,k]+c[M_s,k])}{\varphi_{\frac{\pi}{M_s-1}}(0)} \tag{9}$$

with

$$c_\alpha[k] = C_\alpha \cos\left(\frac{2\pi k}{\alpha}\right),$$

$$s_\alpha[k] = C_\alpha \sin\left(\frac{2\pi k}{\alpha}\right)$$

The relation (6) is obtained by identifying that

$$T_{1,N}\cos(2\pi t) + T_{2,N}\sin(2\pi t)$$

$$= T_{1,N}\sum_{k=0}^{M_t-1} c_{M_t}[k]\varphi_{\frac{2\pi}{M_t},per}(M_t t - k) + T_{2,N}\sum_{k=0}^{M_t-1} s_{M_t}[k]\varphi_{\frac{2\pi}{M_t},per}(M_t t - k) \tag{10}$$

$$= (M_s-1)\sum_{l=-1}^{M_s}\sum_{k=0}^{M_t-1} c[l,k]\varphi_{\frac{2\pi}{M_t},per}(M_t t-k)\varphi'_{\frac{\pi}{M_s-1}}(-l) \tag{11}$$

$$= (M_s-1)\sum_{k=0}^{M_t-1} c[0,k]\varphi'_{\frac{\pi}{M_s-1}}(0)\varphi_{\frac{2\pi}{M_t},per}(M_t t-k) + c[-1,k]\varphi'_{\frac{\pi}{M_s-1}}(1)\varphi_{\frac{2\pi}{M_t},per}(M_t t-k) + c[1,k]\varphi'_{\frac{\pi}{M_s-1}}(-1)\varphi_{\frac{2\pi}{M_t},per}(M_t t-k) \tag{12}$$

$$= (M_s-1)\sum_{k=0}^{M_t-1} (c[-1,k]-c[1,k])\varphi'_{\frac{\pi}{M_s-1}}(1)\,\varphi_{\frac{2\pi}{M_t},per}(M_t t-k) \tag{13}$$

First, (10) is the direct expansion of the cosine and sine in the basis $\varphi_\alpha(2)$. Then, (11) is obtained directly from (5). Finally, (12) is obtained by noticing that, because φ_α is supported in $\left[\frac{-3}{2},\frac{3}{2}\right]$, all terms in the sum vanish except for $j = -1,0,1$. The symmetry properties of the basis impose that $\varphi'_\alpha(0) = 0$ and $\varphi'_\alpha(-1) = \varphi'_\alpha(1)$ yielding (13). One obtains (8) in a similar way. The relations (7) and (8) are obtained directly from (3) and (4), respectively. Note that $c[0,k] \neq c_N$ and $c[M_s,k] \neq c_S$ due to the non-interpolatory behavior of φ_α.

For visualization purpose, the continuously defined spline surface can be discretized as $\eta\left(\frac{j}{(M_s-1)R_s+1}, \frac{i}{M_tR_t}\right)$ for $j = 0,\ldots,(M_s-1)R_s$ and $i = 0,\ldots, M_tR_t-1$, with $R_t, R_s \in \mathbb{N}^*$ some user-defined sampling rates (i.e., amount of samples in each interval between successive control points) along *t* and *s*, respectively. In this study, we chose $M_s = 5$, $M_t = 5$, $R_s = 5$, and $R_t = 5$ to optimize smoothing, geometrical accuracy and computation time.

Axes identification

When parametrizing a cell, the identification of the north-south axis is an important design choice. We identified the following strategies:

1. Canonical $\mathbb{R}^3$ basis: The north-south axis is aligned with *z* and control points are placed along ray $sr[k] = \cos\left(\frac{2\pi k}{M_t}\right)x + \sin\left(\frac{2\pi k}{M_t}\right)y$ in the *x*, *y* plane,
2. Custom axis: We determine a rotation matrix *R* and a center (e.g., obtained from the alignment of two embryos) onto which the model can be registered. The north-south axis is aligned with $z' = Rz$ and control points are placed along rays $r[k] = \cos\left(\frac{2\pi k}{M_t}\right)x' + \sin\left(\frac{2\pi k}{M_t}\right)y'$ in the *x*, *y* plane, with $x' = Rx$ and $y' = Ry$.

Data sampling, ray tracing

Considering the surface model (1) and well-defined parametrization axes, interpolation points are identified by ray tracing in order to reconstruct the spline surface from voxel data.

Ray tracing is implemented relying on the 3D Digital Differential Analyzer (DDA) algorithm (*117*). A ray between two floating-point valued positions p_0 and p_1 is defined for $t \geq 0$ as $p_0 + vt$, with $v = p_1 - p_0$. The algorithm is initialized by defining, for each image dimension *d*, the two quantities $t_{d,\max} = \frac{l_d}{v_d}$ and $\delta_d = \frac{\text{sign}(v_d)}{v_d}$. The DDA then proceeds as described by the following algorithm:

Result: Matrix **P** of grid intersection points
begin
  q = ⌊p_0⌋
  P empty matrix
  while q < ⌊p_1⌋ **do**
    $d_{\min} = \text{argmin}\ t_{d,\max}$
    $p_{d_{\min}} = q_{d=d_{\min}} + 1$
    for $d \neq d_{\min}$ **do**
      $p_d = p_{0,d} + t_{d,\max}v_d$
    end
    insert p as new row of **P**
    $q_{d_{\min}} = q_{d_{\min}} + \text{sign}(v_{d_{\min}})$
    $t_{d_{\min},\max} = t_{d_{\min},\max} + \delta_{d_{\min}}$
  end
end

Each step of the algorithm requires *D* floating point comparisons (where *D* is the image dimension) and 2 floating point addition, making it reasonably fast.

In our case, data contain instance segmented volumes and ray tracing is thus carried out to identify sample points on the object surface. In this context, rays are traced in latitude planes, starting from the north-south axis and expanding until the image boundaries. Tracing stops at the first zero-labeled voxel.

Data sampling, interpolation

Given a set of data points $p[j,i] = \eta\left(\frac{j}{(M_s-1)R_s+1}, \frac{i}{M_tR_t}\right)$ on the surface, the corresponding $c[l,k]$ can be estimated by solving the linear system

$$\Phi C = P,$$

where *C* is a $M_t(M_s+2) \times 1$ *control points matrix* with entries $[C]_{k+Mt(l+1)} = c[l,k]$, Φ is a $(M_tR_t)((M_s-1)R_s+1) \times M_t(M_s+2)$ *basis functions matrix* with entries

$$[\Phi]_{i+j(M_tR_t),k+M_t(l+1)} = \varphi_{\frac{2\pi}{M_t},per}\left(\frac{i}{R_t} - k\right)\varphi_{\frac{\pi}{M_s-1}}\left(\frac{j(M_s-1)}{(M_s-1)R_s+1} - l\right)$$

P is a $(M_tR_t)((M_s-1)R_s+1) \times 1$ *data point matrix* with entries $[P]_{i+j(M_tR_t)} = p[j,i]$.

The system is solved for *C* by finding the least-square best solution that minimizes the squared l_2 norm $\|P - \Phi C\|_2^2$. The poles are estimated from c[*l*,*k*], $l = -1,\ldots, M_s$, $k = 0,\ldots, M_t - 1$, relying on (7) and (9) as

$$c_S = \frac{1}{M_t}\sum_{k=0}^{M_t-1}\varphi_{\frac{\pi}{M_s-1}}(0)c[0,k] + \varphi_{\frac{\pi}{M_s-1}}(1)(c[-1,k]+c[1,k]).$$

$$c_S = \frac{1}{M_t}\sum_{k=0}^{M_t-1}\varphi_{\frac{\pi}{M_s-1}}(0)c[M_s-1,k] + \varphi_{\frac{\pi}{M_s-1}}(1)(c[M_s-2,k]+c[M_s,k]).$$

The tangent planes are retrieved from (6) and (8). For the north tangent plane,

$$\begin{cases} T_{1,N}c_{M_t}[k] + T_{2,N}s_{M_t}[k] &= \gamma(c[-1,k]-c[1,k]) \\ T_{1,N}c_{M_t}[k+1] + T_{2,N}s_{M_t}[k+1] &= \gamma(c[-1,k+1]-c[1,k+1]) \end{cases}$$

leading to

$$T_{1,N} = \frac{\gamma}{M_t}\sum_{k=0}^{M_t-1}\frac{s_{M_t}[k+1](c[-1,k]-c[1,k]) - s_{M_t}[k](c[-1,k+1]-c[1,k+1])}{c_{M_t}[k]s_{M_t}[k+1] - s_{M_t}[k]c_{M_t}[k+1]}$$

$$T_{2,N} = \frac{\gamma}{M_t}\sum_{k=0}^{M_t-1}\frac{c_{M_t}[k+1](c[-1,k]-c[1,k]) - c_{M_t}[k](c[-1,k+1]-c[1,k+1])}{c_{M_t}[k+1]s_{M_t}[k] - c_{M_t}[k]s_{M_t}[k+1]},$$

with

$$\gamma = (M_s-1)\varphi'_{\frac{\pi}{M_s-1}}(1).$$

A similar development follows for the south tangent plane.

Time normalization at the 8-cell stage

Time progression through the 8-cell stage was normalized between 0 (first time point with 8 cells) and 1 (last time point with 8 cells).

Pair-wise distance and 2D projection

To compute the geometrical distance between two sets of 3D images, we first generated the

corresponding segmentation S_A and S_B. Second, we used our nearest neighbor algorithm to determine the best transformation matrix (M) and the best list of cell assignments between S_A and S_B. Then we computed the spline parameters for S_A with a North/South axis aligned with the Z-axis of the image, and the spline parameters for S_B with a North/South axis V such that the MV aligned with the Z-axis of the image. Finally, for each pair of assigned cells between S_A and S_B, we computed the squared Euclidean distance (d) between spline parameters with the same latitude/longitude. The final geometrical distance was defined as the sum of all the distances d, divided by 10,000 for visual clarity.

The projection was done using the implementation of the t-SNE algorithm found in scikit-learn (*118*). Although the t-SNE algorithm tries to keep close objects nearby after projection, it may not always be possible. Because of that, some embryos may be split in two or more smaller clusters after projection, while being one single cluster in high dimensional space (e.g., the long lines crossing the projected morphomap in Fig. 2B). We adjusted the parameters of the t-SNE projection to be as representative as possible of the high dimensional space, however, the 2D projection, including the isolines in Figs. 2B,F,G, 3B, 5E, S5I and S7C,D, should only be used as a visual aid.

The morphomap pipeline was implemented in the Python package morphomap (see section Code availability).

Measurement of the parameter α

To determine the α-parameter, we used the segmentation data. We developed the Python package interfaces (see section Code availability) to determine the angle between two cells, and the corresponding value of α. First, we identified all the voxels on the surface of the embryo (V_S, nonzero voxels with 6-connected neighbors of exactly 2 voxel types, itself and zero), all the voxels on the external line interface between two cells (V_L, nonzero voxels with 6-connected neighbors of exactly 3 different voxel types, itself, zero and a third arbitrary value) and all the voxels belonging to the external interface between three cells or more (V_P, nonzero voxels with 6-connected neighbors of at least 4 different voxels types, itself, zero and other arbitrary values). We defined two parameters: the exclusion radius R_E and the inclusion radius R_I.

For each points P of V_L, between cell A and B, that is further than R_E away from any points in V_P, we listed all the points P_A and P_B of V_S that are within a R_I distance from P and belongs to cell A and B respectively. We fitted two plans such that P belongs to them and the Euclidean distance to P_A and P_B is minimized. Finally, we computed the angle between the two plans and determined the α-parameter using the Young-Dupré equation as previously described (*40*). R_E (20 voxels) and R_I (15 voxels) values were optimized to accurately described theoretical data with known α-parameter.

Estimation of contacts and surface areas

To estimate the surface area, we used our Python package interfaces (see section Code availability) and we triangulated the voxels belonging to the surface of interest using a marching cube algorithm (*119*) and the surface area measurement implemented in scikit-image (*120*). Using the segmentation data, the interface between two cells was defined as the list of nonzero voxels with 6-connected neighbors of exactly 2 voxel types. Note that the interface between a cell and the background is included (one voxel type being zero). The triangulation was performed on the whole cells, but only the triangles less than 2 voxels away from the interface were used in the estimation of the surface area. The interface surface areas were linearly corrected to ensure that the sum of all the interface surface areas equals the estimated surface of the whole cell.

Identification of the closest rigid packing

Rigid packings are named using the Schoenflies notation which characterises the packing according to its internal symmetries. A number between parenthesis is added to differentiate packings sharing the same Schoenflies notation. Identification of the closest rigid packing is available as a python package rbb (see section Code availability).

Preliminaries

1. With 4 hard spheres, we refer to the only possible minimally rigid packing as the ideal packing, as described in ref. (*47*);

2. With 8 hard spheres, we refer to the 13 possible minimally rigid packings as the 13 ideal packings, as described in ref. (*47*);

3. Data of cell contacts is provided as a matrix where the two indices of each position represent the labeling of the two cells in potential contact;

4. The entries of the matrix display the proportion of the surface area of the first cell involved in the contact with the second cell.

While it is theoretically possible to classify the topologies with 16 hard spheres and more, the number of rigid topologies increases super-exponentially with the number of cells (*121*), and further conceptual and technical advancements are required to perform such exhaustive classification.

Rigidity condition

Prior to any computation, we perform a first check whether the topological structure under study is rigid or floppy. In rigid structures, no independent movements of the elements are allowed unless we perform some work over the system (*46*) (see also fig. S3A). For three dimensions, the condition of rigidity for a system with n elements and k constraints (in our case, links) states that:

1. $k \geq 3n - 6$ which, in the case of $n = 8$ implies that $k \geq 18$ that is, that the network of cell cell-contacts has at least 18 links,

2. No node of the network has less than three links. That means that no cell of the packing is in contact to less than 3 other cells.

Distance between two arbitrary packings

To evaluate the distance between two packings we must consider the adjacency matrix of the network describing the topological structure of the packing. Given a packing made of V. cells $(\upsilon_1, \cdots, \upsilon_8)$, the values of the adjacency matrix A of the packing are defined such that $A_{ij} = 1$ if cell υ_i d υ_j are in contact and $A_{ij} = 0$ otherwise. Given that there are $8! = 40320$ different ways to label the cells leading to the same topological structure, the direct comparison of adjacency matrices is not affordable. Furthermore, one must consider that soft spheres may define contacts in places where hard spheres cannot, making the space of possible equivalent configurations even bigger. Therefore, it is much more suitable to work with the ordered spectrum of eigenvalues, which is invariant under permutation of the adjacency matrices. Since, by construction, the adjacency matrix is symmetric and made of nonnegative real entries, the eigenvalue spectrum is all made of real numbers. Thanks to this last property, one can easily compute the distance between two packings: The vector representing the eigenvalue spectrum of the adjacency matrix A is defined as $u_A = (\lambda_1, ..., \lambda_8)$ where $\lambda_1 > \lambda_2 > ... > \lambda_8$. Consider that these two packings can be represented by adjacency matrices A and A', respectively. The distance between these two packings is obtained by considering the Euclidean distance between the vectors representing the (ordered) eigenvalue spectrum of each:

$$d(u_A, u_{A'}) = \sqrt{\sum_{i=1}^{8} \left(\lambda_i - \lambda_i^{'}\right)^2},$$

where

$$u_A = (\lambda_1, ..., \lambda_8) \text{ and } u_{A'} = \left(\lambda_1^{'}, ..., \lambda_8^{'}\right).$$

Finding the closest ideal packing to the real embryo packing

To identify the closest ideal packing to the topological structure of the embryo under study, we proceed as follows:

1. Count the number k of nonzero contacts in the matrix;

2. If $k = 3n - 6$, with n as the number of cells, go to step 3, otherwise set the smallest contact area of the matrix to 0 and go to step 1;

3. Set all nonzero contacts of the matrix to 1 (binarization);

4. Compute the distance to all 13 ideal rigid packings as described above;
5. Pick the closest ideal packing.

Enumeration of topological transitions

A topological transition was defined as two consecutive time points with different identified closest minimally rigid packing. Temporary transitions lasting one time point were ignored from the analysis unless the identified topologies right before and right after were different. For example, the sequence AABABB (three transitions, with A and B two arbitrary topologies) was transformed to AAAABB (one transition), while the sequence AABCC (2 transitions, with C as a third arbitrary topology) was not modified.

Inner/outer cell classification

Cells at the 8-cell stage were all considered outer. For the 16-cell stage, we computed the contact-free area (i.e., the surface area of the cell that is not in contact with another cell) and binned the cells in 10 groups from 0% (completely inside) to approximately 60% (most of the cell surface exposed to the outside environment). The resulting count histogram exhibited a bimodal distribution. We fitted the histogram values with the sum of two weighted Gaussian distributions. The cutoff between inner and outer cells was defined as the value of contact-free surface area at which the two gaussians intersect.

Measurement of the packing parameter

We first determine the centroid c_i of the outer cells i. We then used the average coordinates of outer cells' centroid to obtain the centroid of the embryo e. For every outer cell, we computed the Euclidean distance d_i from c_i to e. The packing parameter was defined as the invert of the standard deviation of $\{d_1, d_2 \ldots d_i\}$(see fig. S6B for a graphical representation of the packing parameter). The packing parameter at the 8-cell stage was measured at approximatively 80% of the intermitotic period (Fig. 6, G and H, and Fig. 7B) or at every available time point (Fig. 6, I and J). The packing parameter at the 16-cell stage was measured two hours after the beginning of the intermitotic period (Fig. 7, B, C, and F, and fig. S7, D and E).

Count of ectopic Sox2+ and Cdx2+ cells

For the early blastocyst stage, fate-based cell type was determined as $Sox2^+$ ($Cdx2^+$ respectively) if the immunostaining signal intensity for Sox2 (Cdx2) was higher than the one for Cdx2 (Sox2). $Sox2^+$ and $Cdx2^+$ cells were labeled as *inner* and *outer* respectively, based on fate markers.

Additionally, we computed the α-shape of the cell centers (*122*) using the R package *alphashape3d* (*123*) and labeled the cells as *outer* and *inner* if they belongs to the surface determined by the α-shape or not, respectively. Ectopic cells are, by definition, cells with label discrepancies between fate markers and their positions in the embryo. Embryos with no identified *inner* or *outer* cells based on marker signal intensity and/or cell coordinates were excluded from the analysis.

Dataset usage

Use of live imaging datasets in figures is described in table S2.

Code availability

Code used to produce the figure panels and the analyses in this study is available at Zenodo (*124*).

Statistical Analysis

All statistical analyses were performed using RStudio 2022.12.0+353 (*125*) with R 4.2.2 (*126*), with the base library and the following libraries: *alphashape3d* (*123*), *ggplot2* (*127*), *ggrepel* (*128*) and *namespace* (*129*). No statistical analysis was used to predetermine sample size. No sample was excluded. No randomization method was used. The investigators were not blinded during experiments. Sample sizes, statistical tests, and *P*-values are indicated in the text, figures, and figure legends. *n*-values indicate number of embryos analyzed for different experimental conditions unless mentioned otherwise. Error bars indicate mean ± s.d. unless mentioned otherwise.

REFERENCES AND NOTES

1. J. R. Chubb, Symmetry breaking in development and stochastic gene expression *Wiley Interdiscip. Rev. Dev. Biol.* **6**, e284 (2017). doi: 10.1002/wdev.284
2. A. Raj, A. van Oudenaarden, Nature, nurture, or chance: Stochastic gene expression and its consequences. *Cell* **135**, 216–226 (2008). doi: 10.1016/j.cell.2008.09.050; pmid: 18957198
3. A. Eldar, M. B. Elowitz, Functional roles for noise in genetic circuits. *Nature* **467**, 167–173 (2010). doi: 10.1038/nature09326; pmid: 20829787
4. G. Balázsi, A. van Oudenaarden, J. J. Collins, Cellular decision making and biological noise: From microbes to mammals. *Cell* **144**, 910–925 (2011). doi: 10.1016/j.cell.2011.01.030; pmid: 21414483
5. M. R. Spratt, K. Lane, Navigating Environmental Transitions: The Role of Phenotypic Variation in Bacterial Responses. *mBiol.* **13**, e02212–22 (2022). doi: 10.1128/mbio.02212-22; pmid: 36259726
6. H. Maamar, A. Raj, D. Dubnau, Noise in gene expression determines cell fate in *Bacillus subtilis*. *Science* **317**, 526–529 (2007). doi: 10.1126/science.1140818; pmid: 17569828
7. G. M. Süel, R. P. Kulkarni, J. Dworkin, J. Garcia-Ojalvo, M. B. Elowitz, Tunability and noise dependence in differentiation dynamics. *Science* **315**, 1716–1719 (2007). doi: 10.1126/science.1137455; pmid: 17379809
8. H. H. Chang, M. Hemberg, M. Barahona, D. E. Ingber, S. Huang, Transcriptome-wide noise controls lineage choice in mammalian progenitor cells. *Nature* **453**, 544–547 (2008). doi: 10.1038/nature06965; pmid: 18497826
9. H. M. Meyer, A. H. K. Roeder, Stochasticity in plant cellular growth and patterning. *Front. Plant Sci.* **5**, 420 (2014). doi: 10.3389/fpls.2014.00420; pmid: 25250034
10. Y. Ohnishi *et al*., Cell-to-cell expression variability followed by signal reinforcement progressively segregates early mouse lineages. *Nat. Cell Biol.* **16**, 27–37 (2014). doi: 10.1038/ncb2881; pmid: 24292013
11. C. S. Simon, A. K. Hadjantonakis, C. Schröter, Making lineage decisions with biological noise: Lessons from the early mouse embryo. *Wiley Interdiscip. Rev. Dev. Biol.* **7**, e319 (2018). doi: 10.1002/wdev.319; pmid: 29709110
12. N. D. Lord *et al*., Stochastic antagonism between two proteins governs a bacterial cell fate switch. *Science* **366**, 116–120 (2019). doi: 10.1126/science.aaw4506; pmid: 31604312
13. A. P. Feinberg, R. Ohlsson, S. Henikoff, The epigenetic progenitor origin of human cancer. *Nat. Rev. Genet.* **7**, 21–33 (2006). doi: 10.1038/nrg1748; pmid: 16369569
14. A. Brock, H. Chang, S. Huang, Non-genetic heterogeneity—A mutation-independent driving force for the somatic evolution of tumours. *Nat. Rev. Genet.* **10**, 336–342 (2009). doi: 10.1038/nrg2556; pmid: 19337290
15. A. P. Feinberg, R. A. Irizarry, Evolution in health and medicine Sackler colloquium: Stochastic epigenetic variation as a driving force of development, evolutionary adaptation, and disease. *Proc. Natl. Acad. Sci. U.S.A.* **107**, 1757–1764 (2010). doi: 10.1073/pnas.0906183107; pmid: 20080672
16. C. C. Bell, O. Gilan, Principles and mechanisms of non-genetic resistance in cancer. *Br. J. Cancer* **122**, 465–472 (2020). doi: 10.1038/s41416-019-0648-6; pmid: 31831859
17. M. A. Koldobskiy *et al*., Converging genetic and epigenetic drivers of paediatric acute lymphoblastic leukaemia identified by an information-theoretic analysis. *Nat. Biomed. Eng.* **5**, 360–376 (2021). doi: 10.1038/s41551-021-00703-2; pmid: 33859388
18. M. Carlson, W. Reeves, M. Veeman, Stochasticity and stereotypy in the Ciona notochord. *Dev. Biol.* **397**, 248–256 (2015). doi: 10.1016/j.ydbio.2014.11.016; pmid: 25459659
19. R. Dumollard *et al*., The invariant cleavage pattern displayed by ascidian embryos depends on spindle positioning along the cell's longest axis in the apical plane and relies on asynchronous cell divisions. *eLife* **6**, 1–23 (2017). doi: 10.7554/eLife.19290; pmid: 28121291
20. L. Hong *et al*., Variable Cell Growth Yields Reproducible OrganDevelopment through Spatiotemporal Averaging. *Dev. Cell* **38**, 15–32 (2016). doi: 10.1016/j.devcel.2016.06.016; pmid: 27404356
21. L. Hong *et al*., Heterogeneity and Robustness in Plant Morphogenesis: From Cells to Organs. *Annu. Rev. Plant Biol.* **69**, 469–495 (2018). doi: 10.1146/annurev-arplant-042817-040517; pmid: 29505739
22. P. A. Haas, S. S. M. H. Höhn, A. R. Honerkamp-Smith, J. B. Kirkegaard, R. E. Goldstein, The noisy basis of morphogenesis: Mechanisms and mechanics of cell sheet folding inferred from developmental variability. *PLOS Biol.* **16**, e2005536 (2018). doi: 10.1371/journal.pbio.2005536; pmid: 30001335
23. A. Yanagida *et al*., Cell surface fluctuations regulate early embryonic lineage sorting. *Cell* **185**, 777–793.e20 (2022). doi: 10.1016/j.cell.2022.01.022; pmid: 35196500
24. L. Bromham, What can DNA Tell us About the Cambrian Explosion? *Integr. Comp. Biol.* **43**, 148–156 (2003). doi: 10.1093/icb/43.1.148; pmid: 21680419
25. J. Draghi, Phenotypic variability can promote the evolution of adaptive plasticity by reducing the stringency of natural selection. *J. Evol. Biol.* **32**, 1274–1289 (2019). doi: 10.1111/jeb.13527; pmid: 31479539
26. M. Schmid, M. Paniw, M. Postuma, A. Ozgul, F. Guillaume, A Trade-Off between Robustness to Environmental Fluctuations and Speed of Evolution. *Am. Nat.* **200**, E16–E35 (2022). doi: 10.1086/719654; pmid: 35737989
27. U. Hernández, L. Posadas-Vidales, C. Espinosa-Soto, On the effects of the modularity of gene regulatory networks on phenotypic variability and its association with robustness. *Biosystems* **212**, 104586 (2022). doi: 10.1016/j.biosystems.2021.104586; pmid: 34971735
28. J.-E. Dietrich, T. Hiiragi, Stochastic patterning in the mouse pre-implantation embryo. *Development* **134**, 4219–4231 (2007). doi: 10.1242/dev.003798; pmid: 17978007
29. R. M. Roberts, M. Katayama, S. R. Magnuson, M. T. Falduto, K. E. O. Torres, Transcript profiling of individual twin blastomeres derived by splitting two-cell stage murine embryos. *Biol. Reprod.* **84**, 487–494 (2011). doi: 10.1095/biolreprod.110.086884; pmid: 21076082
30. I. Lavagi *et al*., Single-cell RNA sequencing reveals developmental heterogeneity of blastomeres during major genome activation in bovine embryos. *Sci. Rep.* **8**, 4071 (2018). doi: 10.1038/s41598-018-22248-2; pmid: 29511234
31. S. Louvet-Vallée, S. Vinot, B. Maro, Mitotic spindles and cleavage planes are oriented randomly in the two-cell mouse

embryo. *Curr. Biol.* **15**, 464–469 (2005). doi: 10.1016/j.cub.2004.12.078; pmid: 15753042

32. S. J. Kelly, J. G. Mulnard, C. F. Graham, Cell division and cell allocation in early mouse development. *J. Embryol. Exp. Morphol.* **48**, 37–51 (1978). doi: 10.1242/dev.48.1.37; pmid: 581768
33. D. Mashiko *et al*., Asynchronous division at 4-8-cell stage of preimplantation embryos affects live birth through ICM/TE differentiation. *Sci. Rep.* **12**, 9411 (2022). doi: 10.1038/s41598-022-13646-8; pmid: 35672442
34. C. E. M. Aiken, P. P. L. Swoboda, J. N. Skepper, M. H. Johnson, The direct measurement of embryogenic volume and nucleo-cytoplasmic ratio during mouse pre-implantation development. *Reproduction* **128**, 527–535 (2004). doi: 10.1530/rep.1.00281; pmid: 15509698
35. J.-L. Maître *et al*., Asymmetric division of contractile domains couples cell positioning and fate specification. *Nature* **536**, 344–348 (2016). doi: 10.1038/nature18958; pmid: 27487217
36. C. R. Samarage *et al*., Cortical Tension Allocates the First Inner Cells of the Mammalian Embryo. *Dev. Cell* **34**, 435–447 (2015). doi: 10.1016/j.devcel.2015.07.004; pmid: 26279486
37. E. Korotkevich *et al*., The Apical Domain Is Required and Sufficient for the First Lineage Segregation in the Mouse Embryo. *Dev. Cell* **40**, 235–247.e7 (2017). doi: 10.1016/j.devcel.2017.01.006; pmid: 28171747
38. P. Bowman, A. McLaren, Cleavage rate of mouse embryos *in vivo* and *in vitro*. *J. Embryol. Exp. Morphol.* **24**, 203–207 (1970). doi: 10.1242/dev.24.1.203; pmid: 5487156
39. R. Delgado-Gonzalo, N. Chenouard, M. Unser, Spline-based deforming ellipsoids for interactive 3D bioimage segmentation. *IEEE Trans. Image Process.* **22**, 3926–3940 (2013). doi: 10.1109/TIP.2013.2264680; pmid: 23708807
40. J.-L. Maître, R. Niwayama, H. Turlier, F. Nédélec, T. Hiiragi, Pulsatile cell-autonomous contractility drives compaction in the mouse embryo. *Nat. Cell Biol.* **17**, 849–855 (2015). doi: 10.1038/ncb3185; pmid: 26075357
41. J. I. Alsous, P. Villoutreix, N. Stoop, S. Y. Shvartsman, J. Dunkel, Entropic effects in cell lineage tree packings. *Nat. Phys.* **14**, 1016–1021 (2018). doi: 10.1038/s41567-018-0202-0; pmid: 30881478
42. N. I. Petridou, B. Corominas-Murtra, C.-P. Heisenberg, E. Hannezo, Rigidity percolation uncovers a structural basis for embryonic tissue phase transitions. *Cell* **184**, 1914–1928. e19 (2021). doi: 10.1016/j.cell.2021.02.017; pmid: 33730596
43. J. Giammona, O. Campàs, Physical constraints on early blastomere packings. *PLOS Comput. Biol.* **17**, e1007994 (2021). doi: 10.1371/journal.pcbi.1007994; pmid: 33497383
44. X. Kuang *et al*., Computable early Caenorhabditis elegans embryo with a phase field model. *PLOS Comput. Biol.* **18**, e1009755 (2022). doi: 10.1371/journal.pcbi.1009755; pmid: 35030161
45. D. J. Skinner, H. Jeckel, A. C. Martin, K. Drescher, J. Dunkel, Topological packing statistics of living and nonliving matter. *Sci. Adv.* **9**, eadg1261 (2023). doi: 10.1126/sciadv.adg1261; pmid: 37672580
46. D. J. Jacobs, Generic rigidity in three-dimensional bond-bending networks. *J. Phys. Math. Gen.* **31**, 6653–6668 (1998). doi: 10.1088/0305-4470/31/31/012
47. N. Arkus, V. N. Manoharan, M. P. Brenner, Minimal energy clusters of hard spheres with short range attractions. *Phys. Rev. Lett.* **103**, 118303 (2009). doi: 10.1103/PhysRevLett.103.118303; pmid: 19792406
48. N. Arkus, V. N. Manoharan, M. P. Brenner, Deriving Finite Sphere Packings. *SIAM J. Discrete Math.* **25**, 1860–1901 (2011). doi: 10.1137/100784424
49. B. K. Vaĭnshteĭn, Ed., *Modern Crystallography* (Springer, 1994).
50. N. S. Goel, C. F. Doggenweiler, R. L. Thompson, Simulation of cellular compaction and internalization in mammalian embryo development as driven by minimization of surface energy. *Bull. Math. Biol.* **48**, 167–187 (1986). doi: 10.1016/S0092-8240(86)80005-2; pmid: 3719154
51. T. Hayashi, R. W. Carthew, Surface mechanics mediate pattern formation in the developing retina. *Nature* **431**, 647–652 (2004). doi: 10.1038/nature02952; pmid: 15470418
52. A. Pierre, J. Sallé, M. Wühr, N. Minc, Generic Theoretical Models to Predict Division Patterns of Cleaving Embryos. *Dev. Cell* **39**, 667–682 (2016). doi: 10.1016/j.devcel.2016.11.018; pmid: 27997824
53. C.-P. Heisenberg, D'Arcy Thompson's 'on Growth and form': From soap bubbles to tissue self-organization. *Mech. Dev.* **145**, 32–37 (2017). doi: 10.1016/j.mod.2017.03.006; pmid: 28442367
54. K. A. Brakke, The Surface Evolver. *Exp. Math.* **1**, 141–165 (1992). doi: 10.1080/10586458.1992.10504253
55. P. Marmottant *et al*., The role of fluctuations and stress on the effective viscosity of cell aggregates. *Proc. Natl. Acad. Sci. U.S.A.* **106**, 17271–17275 (2009). doi: 10.1073/pnas.0902085106; pmid: 19805170
56. D. Bi, J. H. Lopez, J. M. Schwarz, M. L. Manning, Energy barriers and cell migration in densely packed tissues. *Soft Matter* **10**, 1885–1890 (2014). doi: 10.1039/c3sm52893f; pmid: 24652538
57. D. Bi, X. Yang, M. C. Marchetti, M. L. Manning, Motility-driven glass and jamming transitions in biological tissues. *Phys. Rev. X* **6**, 021011 (2016). doi: 10.1103/PhysRevX.6.021011; pmid: 28966874
58. D. Pinheiro, R. Kardos, É. Hannezo, C.-P. Heisenberg, Morphogen gradient orchestrates pattern-preserving tissue morphogenesis via motility-driven unjamming. *Nat. Phys.* **18**, 1482–1493 (2022). doi: 10.1038/s41567-022-01787-6
59. B. H. Várkuti *et al*., A highly soluble, non-phototoxic, non-fluorescent blebbistatin derivative. *Sci. Rep.* **6**, 26141 (2016). doi: 10.1038/srep26141; pmid: 27241904
60. R. L. Gardner, Experimental analysis of second cleavage in the mouse. *Hum. Reprod.* **17**, 3178–3189 (2002). doi: 10.1093/humrep/17.12.3178; pmid: 12456621
61. R. Van Haarlem, R. Van Wijk, A. H. M. Fikkert, Analysis of the variability in cleavage times and demonstration of a mitotic gradient during the cleavage stages of Nothobranchius guentheri. *Cell Tissue Kinet.* **14**, 285–300 (1981). doi: 10.1111/j.1365-2184.1981.tb00533.x; pmid: 7237515
62. C. Roux, R. Borodkine, C. Joanne, J. L. Bresson, G. Agnani, Morphological classification of human in-vitro fertilization embryos based on the regularity of the asynchronous division process. *Hum. Reprod. Update* **1**, 488–496 (1995). doi: 10.1093/humupd/1.5.488; pmid: 9080222
63. N. Olivier *et al*., Cell lineage reconstruction of early zebrafish embryos using label-free nonlinear microscopy. *Science* **329**, 967–971 (2010). doi: 10.1126/science.1189428; pmid: 20724640
64. R. Dumollard, C. Hebras, L. Besnardeau, A. McDougall, Beta-catenin patterns the cell cycle during maternal-to-zygotic transition in urochordate embryos. *Dev. Biol.* **384**, 331–342 (2013). doi: 10.1016/j.ydbio.2013.10.007; pmid: 24140189
65. P. Villoutreix *et al*., An integrated modelling framework from cells to organism based on a cohort of digital embryos. *Sci. Rep.* **6**, 37438 (2016). doi: 10.1038/srep37438; pmid: 27910875
66. G. A. Anderson, L. Gelens, J. C. Baker, J. E. Ferrell Jr., Desynchronizing Embryonic Cell Division Waves Reveals the Robustness of Xenopus laevis Development. *Cell Rep.* **21**, 37–46 (2017). doi: 10.1016/j.celrep.2017.09.017; pmid: 28978482
67. J. Sallé, N. Minc, Cell division geometries as central organizers of early embryo development. *Semin. Cell Dev. Biol.* **130**, 3–11 (2022). doi: 10.1016/j.semcdb.2021.08.004; pmid: 34419349
68. O. Tassy, F. Daian, C. Hudson, V. Bertrand, P. Lemaire, A quantitative approach to the study of cell shapes and interactions during early chordate embryogenesis. *Curr. Biol.* **16**, 345–358 (2006). doi: 10.1016/j.cub.2005.12.044; pmid: 16488868
69. C. Ducroz, J.-C. Olivo-Marin, A. Dufour, "Characterization of cell shape and deformation in 3D using Spherical Harmonics" in 2012 9th IEEE International Symposium on Biomedical Imaging (ISBI) (IEEE, 2012), pp. 848–851.
70. R. Tournemenne, C. Ducroz, J.-C. Olivo-Marin, A. Dufour, "3D shape analysis using overcomplete spherical wavelets: Application to BLEB detection in cell biology" in 2014 IEEE 11th International Symposium on Biomedical Imaging (ISBI) (IEEE, 2014), pp. 365–368.
71. M. Saad, I. H. Lee, T.-S. Choi, Are shape morphologies associated with survival? A potential shape-based biomarker predicting survival in lung cancer. *J. Cancer Res. Clin. Oncol.* **145**, 2937–2950 (2019). doi: 10.1007/s00432-019-03048-1; pmid: 31620897
72. L. Guignard *et al*., Contact area-dependent cell communication and the morphological invariance of ascidian embryogenesis. *Science* **369**, eaar5663 (2020). doi: 10.1126/science.aar5663; pmid: 32646972
73. M. Agus, E. Gobbetti, G. Pintore, C. Cali, J. Schneider, "WISH: Efficient 3D biological shape classification through Willmore flow and Spherical Harmonics decomposition" in 2020 IEEE/CVF Conference on Computer Vision and Pattern Recognition Workshops (CVPRW) (IEEE, 2020), pp. 4184–4194.
74. R. Xiong, K. Sugioka, Improved 3D cellular morphometry of Caenorhabditis elegans embryos using a refractive index matching medium. *PLOS ONE* **15**, e0238955 (2020). doi: 10.1371/journal.pone.0238955; pmid: 32997668
75. T. G. R. Andrews, W. Pönisch, E. K. Paluch, B. J. Steventon, E. Benito-Gutierrez, Single-cell morphometrics reveals ancestral principles of notochord development. *Development* **148**, dev199430 (2021). doi: 10.1242/dev.199430; pmid: 34343262
76. G. Valizadeh, F. Babapour Mofrad, A Comprehensive Survey on Two and Three-Dimensional Fourier Shape Descriptors: Biomedical Applications. *Arch. Comput. Methods Eng.* **29**, 4643–4681 (2022). doi: 10.1007/s11831-022-09750-7
77. L. M. G. Paim, G. FitzHarris, Cell size and polarization determine cytokinesis furrow ingression dynamics in mouse embryos. *Proc. Natl. Acad. Sci. U.S.A.* **119**, e2119381119 (2022). doi: 10.1073/pnas.2119381119; pmid: 35294282
78. G. Froese, The distribution and interdependence of generation times of HeLa cells. *Exp. Cell Res.* **35**, 415–419 (1964). doi: 10.1016/0014-4827(64)90108-9; pmid: 14195449
79. O. Sandler *et al*., Lineage correlations of single cell division time as a probe of cell-cycle dynamics. *Nature* **519**, 468–471 (2015). doi: 10.1038/nature14318; pmid: 25762143
80. M. Soltani, C. A. Vargas-Garcia, D. Antunes, A. Singh, Intercellular Variability in Protein Levels from Stochastic Expression and Noisy Cell Cycle Processes. *PLOS Comput. Biol.* **12**, e1004972 (2016). doi: 10.1371/journal.pcbi.1004972; pmid: 27536771
81. H. Y. G. Lim *et al*., Keratins are asymmetrically inherited fate determinants in the mammalian embryo. *Nature* **585**, 404–409 (2020). doi: 10.1038/s41586-020-2647-4; pmid: 32848249
82. S. Seirin-Lee, K. Yamamoto, A. Kimura, The extra-embryonic space and the local contour are crucial geometric constraints regulating cell arrangement. *Development* **149**, dev200401 (2022). doi: 10.1242/dev.200401; pmid: 35552395
83. P. Hänggi, Stochastic resonance in biology. How noise can enhance detection of weak signals and help improve biological information processing. *ChemPhysChem* **3**, 285–290 (2002). doi: 10.1002/1439-7641(20020315)3:3<285::AID-CPHC285>3.0.CO;2-A; pmid: 12503175
84. T. Betz, D. Koch, D. Lim, J. A. Käs, Stochastic Actin Polymerization and Steady Retrograde Flow Determine Growth Cone Advancement. *Biophys. J* **96**, 5130–5138 (2009). doi: 10.1016/j.bpj.2009.03.045; pmid: 19527673
85. M. A. Coomer, L. Ham, M. P. H. Stumpf, Noise distorts the epigenetic landscape and shapes cell-fate decisions. *Cell Syst.* **13**, 83–102.e6 (2022). doi: 10.1016/j.cels.2021.09.002; pmid: 34626539
86. W. Horsthemke, R. Lefever, *Noise-Induced Transitions* (Springer, 2006); Springer Series in Synergetics, vol 15.
87. N. G. van Kampen, *Stochastic Processes in Physics and Chemistry* (Elsevier, 2007).
88. Y. Z. Tsypkin, *Adaptation and Learning in Automatic Systems* (Academic Press, 1971).
89. L. Bottou, N. Murata, "Stochastic Approximations and Efficient Learning" in *The Handbook of Brain Theory and Neural Networks*, M. A. Arbib, Ed. (MIT Press, Cambridge, MA, Second edition, 2002), pp. 1108–1122.
90. H. Koyama, H. Suzuki, X. Yang, S. Jiang, R. H. Foote, Analysis of polarity of bovine and rabbit embryos by scanning electron microscopy. *Biol. Reprod.* **50**, 163–170 (1994). doi: 10.1095/biolreprod50.1.163; pmid: 8312441
91. F. Sultana, M. Hatori, N. Shimozawa, T. Ebisawa, T. Sankai, Continuous observation of rabbit preimplantation embryos in vitro by using a culture device connected to a microscope. *J. Am. Assoc. Lab. Anim. Sci.* **48**, 52–56 (2009). pmid: 19245751
92. A. C. Enders, K. C. Lantz, S. Schlafke, The morula-blastocyst transition in two Old World primates: The baboon and rhesus monkey. *J. Med. Primatol.* **19**, 725–747 (1990). doi: 10.1111/j.1600-0684.1990.tb00477.x; pmid: 2084262
93. M. D. Muzumdar, B. Tasic, K. Miyamichi, L. Li, L. Luo, A global double-fluorescent Cre reporter mouse. *Genesis* **45**, 593–605 (2007). doi: 10.1186/1472-6750-4-33; pmid: 15619330
94. A.-K. Hadjantonakis, V. E. Papaioannou, Dynamic in vivo imaging and cell tracking using a histone fluorescent protein fusion in mice. *BMC Biotechnol.* **4**, 33 (2004). doi: 10.1186/1472-6750-4-33; pmid: 15619330
95. J. Jacobelli *et al*., Confinement-optimized three-dimensional T cell amoeboid motility is modulated via myosin IIA-regulated adhesions. *Nat. Immunol.* **11**, 953–961 (2010). doi: 10.1038/ni.1936; pmid: 20835229

96. W. N. de Vries *et al*., Expression of Cre recombinase in mouse oocytes: A means to study maternal effect genes. *Genesis* **26**, 110–112 (2000). doi: 10.1002/(SICI)1526-968X(200002)26:2<110::AID-GENE2>3.0.CO;2-8; pmid: 10686600
97. T. Tsukiyama *et al*., Monkeys mutant for PKD1 recapitulate human autosomal dominant polycystic kidney disease. *Nat. Commun.* **10**, 5517 (2019). doi: 10.1038/s41467-019-13398-6; pmid: 31822676
98. J. J. Parrish, J. Susko-Parrish, M. A. Winer, N. L. First, Capacitation of bovine sperm by heparin. *Biol. Reprod.* **38**, 1171–1180 (1988). doi: 10.1095/biolreprod38.5.1171; pmid: 3408784
99. S. G. Megason, "In Toto Imaging of Embryogenesis with Confocal Time-Lapse Microscopy" in *Zebrafish*, G. J. Lieschke, A. C. Oates, K. Kawakami, Eds. (Humana Press, 2009) pp. 317–332.
100. K. Yamagata *et al*., Noninvasive visualization of molecular events in the mammalian zygote. *Genesis* **43**, 71–79 (2005). doi: 10.1095/biolreprod63.1.281; pmid: 10859270
101. J. D. Biggers, L. K. McGinnis, M. Raffin, Amino acids and preimplantation development of the mouse in protein-free potassium simplex optimized medium. *Biol. Reprod.* **63**, 281–293 (2000). doi: 10.1095/biolreprod63.1.281; pmid: 10859270
102. Y. Tsunoda, T. Yasui, K. Nakamura, T. Uchida, T. Sugie, Effect of cutting the zona pellucida on the pronuclear transplantation in the mouse. *J. Exp. Zool.* **240**, 119–125 (1986). doi: 10.1002/jez.1402400115; pmid: 3772328
103. E. Faure *et al*., A workflow to process 3D+time microscopy images of developing organisms and reconstruct their cell lineage. *Nat. Commun.* **7**, 8674 (2016). doi: 10.1038/ncomms9674; pmid: 26912388
104. C. Stringer, T. Wang, M. Michaelos, M. Pachitariu, Cellpose: A generalist algorithm for cellular segmentation. *Nat. Methods* **18**, 100–106 (2021). doi: 10.1038/s41592-020-01018-x; pmid: 33318659
105. M. Pachitariu, C. Stringer, Cellpose 2.0: How to train your own model. *Nat. Methods* **19**, 1634–1641 (2022). doi: 10.1038/s41592-022-01663-4; pmid: 36344832
106. M. J. Frisch *et al*., napari: a multi-dimensional image viewer for Python, version v0.4.17rc8, Zenodo (2022); https://doi.org/10.5281/zenodo.3555620.
107. A. Wolny *et al*., Accurate and versatile 3D segmentation of plant tissues at cellular resolution. *eLife* **9**, 1–34 (2020). doi: 10.7554/eLife.57613; pmid: 32723478
108. T. Beier *et al*., Multicut brings automated neurite segmentation closer to human performance. *Nat. Methods* **14**, 101–102 (2017). doi: 10.1038/nmeth.4151; pmid: 28139671
109. S. Wolf *et al*., "The Mutex Watershed: Efficient, Parameter-Free Image Partitioning" in *Computer Vision – ECCV 2018*, V. Ferrari, M. Hebert, C. Sminchisescu, Y. Weiss, Eds. (Springer, 2018), pp. 571–587.
110. J. Funke *et al*., Large Scale Image Segmentation with Structured Loss Based Deep Learning for Connectome Reconstruction. *IEEE Trans. Pattern Anal. Mach. Intell.* **41**, 1669–1680 (2019). doi: 10.1109/TPAMI.2018.2835450; pmid: 29993708
111. N. Bansal, A. Blum, S. Chawla, Correlation Clustering. *Mach. Learn.* **56**, 89–113 (2004). doi: 10.1023/B:MACH.0000033116.57574.95
112. B. Andres, J. H. Kappes, T. Beier, U. Kothe, F. A. Hamprecht, "Probabilistic image segmentation with closedness constraints" in 2011 International Conference on Computer Vision (IEEE, 2011), pp. 2611–2618.
113. J. H. Kappes, M. Speth, B. Andres, G. Reinelt, C. Schn, "Globally Optimal Image Partitioning by Multicuts" in *Energy Minimization Methods in Computer Vision and Pattern Recognition*, Y. Boykov, F. Kahl, V. Lempitsky, F. R. Schmidt, Eds. (Springer, 2011), pp. 31–44.
114. C. Pape *et al*., "Solving Large Multicut Problems for Connectomics via Domain Decomposition" in 2017 IEEE International Conference on Computer Vision Workshops (ICCVW) (IEEE, 2017), pp. 1–10.
115. J. Schindelin *et al*., Fiji: An open-source platform for biological-image analysis. *Nat. Methods* **9**, 676–682 (2012). doi: 10.1038/nmeth.2019; pmid: 22743772
116. R. Delgado-Gonzalo, P. Thévenaz, M. Unser, Exponential splines and minimal-support bases for curve representation. *Comput. Aided Geom. Des.* **29**, 109–128 (2012). doi: 10.1016/j.cagd.2011.10.005
117. J. Amanatides, A. Woo, A Fast Voxel Traversal Algorithm for Ray Tracing. *Eurographics* **87**, 3–10 (1987).
118. F. Pedregosa *et al*., Scikit-learn: Machine Learning in Python. *JMLR* **12**, 2825–2830 (2011).
119. T. Lewiner, H. Lopes, A. W. Vieira, G. Tavares, Efficient Implementation of Marching Cubes' Cases with Topological Guarantees. *J. Graphics Tools* **8**, 1–15 (2003). doi: 10.1080/10867651.2003.10487582
120. S. van der Walt *et al*., scikit-image: Image processing in Python. *PeerJ* **2**, e453 (2014). doi: 10.7717/peerj.453; pmid: 25024921
121. M. C. Holmes-Cerfon, Enumerating Rigid Sphere Packings. *SIAM Rev.* **58**, 229–244 (2016). doi: 10.1137/140982337
122. H. Edelsbrunner, E. P. Mücke, Three-dimensional alpha shapes. *ACM Trans. Graph.* **13**, 43–72 (1994). doi: 10.1145/174462.156635
123. T. Lafarge, B. Pateiro-Lopez, alphashape3d: Implementation of the 3D Alpha-Shape for the Reconstruction of 3D Sets from a Point Cloud, version 1.3.1 (2020); https://CRAN.R-project.org/package=alphashape3d.
124. D. Fabrèges *et al*., Temporal variability and cell mechanics control robustness in mammalian embryogenesis, version 1.0, Zenodo (2024); https://doi.org/10.5281/ZENODO.12819781.
125. Posit team, RStudio: Integrated Development Environment for R, version 2022.12.0+353, Posit Software, PBC (2022); http://www.posit.co/.
126. R Core Team, R: A Language and Environment for Statistical Computing, version 4.2.2, R Foundation for Statistical Computing (2022); https://www.R-project.org/.
127. H. Wickham, *Ggplot2: Elegant Graphics for Data Analysis* (Springer, 2016)
128. K. Slowikowski *et al*., ggrepel: Automatically Position Non-Overlapping Text Labels with "ggplot2," version 0.9.2 (2022); https://CRAN.R-project.org/package=ggrepel.
129. W. Chang, D. Adler, H. Wickham, G. R. Warnes, namespace: Provide namespace managment functions not (yet) present in base R, version 0.9.1 (2012); https://CRAN.R-project.org/package=namespace.

ACKNOWLEDGMENTS

We are grateful to the members of the Hiiragi laboratory for discussions and comments on the manuscript: R. Bloehs, S. Friese, S. Hozeifi, L. Pérez, and W. Schwarzer for their technical support; V. Janssen for establishing the PAB protocol; members of the Tsukiyama group for the animal care with monkeys, in particular H. Tsuchiya and M. Nakaya; Unité Commune d'Expérimentation Animale (UCEA, Jouy-en-Josas, France) for the animal care with rabbits; the EMBL electronic and mechanical workshops and the EMBL animal facility for their support; We thank Luxendo for the close collaboration in developing the light-sheet microscopy for mammalian embryos. **Funding:** This work was funded by the following: EMBL Interdisciplinary Postdoc Program (EIPOD) under Marie Sklodowska Curie Actions COFUND III RTD (to D.F.); JSPS Overseas Research Fellowship (to T.I.); Field of excellence "Complexity of life in basic research and innovation" of the University of Graz (to B.C.M.); European Research Council, ERC Advanced Grant "SelforganisingEmbryo", grant agreement 742732; ERC Advanced Grant "COORDINATION" grant agreement 101055287 (to T.H.); Stichting LSH-TKI, grant LSHM21020 (to T.H.) JSPS KAKENHI grants JP21H05038 and JP22H05166 (to T.H.)
Author contributions: Conceptualization: D.F., B.C.M., E.H., and T.H. Methodology: D.F., B.C.M., A.K.r., V.U., E.H., and T.H. Software programming: D.F., B.C.M., A.W., V.U. Validation: D.F., B.C.M., E.H., and T.H. Formal analysis: D.F. Investigation: D.F., P.M., A.Ki., T.I., C.I., N.D., and T.H. Resources: T.T., A.Kr., V.D., and T.H. data curation: D.F., A.Ki., J.G., and A.S. Writing – original draft: D.F., B.C.M., E.H., and T.H. Writing – review & editing: D.F., B.C.M., A.Ki., V.U., E.H., and T.H. Visualization: D.F. and B.C.M. Supervision: D.F., B.C.M., T.T., A.Kr., V.D., V.U., E.H., and T.H. Project administration: D.F. and T.H. Funding acquisition: D.F. and T.H. **Competing interests:** Authors declare that they have no competing interests. **Data and materials availability:** All original code and data reported in this paper is publicly available as of the date of publication on Zenodo (*124*).

SUPPLEMENTARY MATERIALS

science.org/doi/10.1126/science.adh1145
Figs. S1 to S7
Tables S1 and S2
MDAR Reproducibility Checklist
Movies S1 to S6

Submitted 14 February 2023; resubmitted 2 October 2023
Accepted 20 August 2024
10.1126/science.adh1145